Computed Tomography (CT) Image Quality Analysis Methods, Noise Effect and Calibration

Rahul P. Mahajan
Research and Development Department
Healthcare and Medical Device Development Industry
College of Engineering
Pune, India
rpm.mahajan@gmail.com

0009-0003-3038-4391

***Abstract*—**Commutated tomography (CT) imaging has become more common for medical diagnosis in recent years. Since a correct diagnosis has a substantial impact on patient outcomes and treatment plans, the rapid identification of strokes using CT scans is essential for prompt clinical action. In order to train and evaluate deep learning models, this work made use of a publically available dataset of CT pictures of brain strokes. The collection includes labelled images reflecting various stroke states. Artefacts like as noise and intensity changes are common in CT scans and might make it difficult to classify strokes accurately. In order to overcome these obstacles, four deep learning models, CNN, VGG16, ResNet, and Multilayer Perceptron were used for noise-aware preprocessing in CT images and for stroke identification. To make the model more generalizable and resistant to imaging discrepancies, the preprocessing pipeline included noise reduction methods, intensity normalization, and data augmentation. The F1-score (F1), recall (REC), accuracy (ACC), and precision (PRE) were utilized for a comprehensive evaluation of the classification abilities. With a remarkable 99.50% accuracy, convolutional neural networks (CNNs) were able to extract spatial and hierarchical information from noisy images. ResNet came in second with 97.75%, VGG16 third with 96.50%, and MLP fourth with 96%. These results demonstrate the importance of preprocessing and noise handling in enhancing classification reliability. The proposed framework shows promise for real-time clinical deployment, supporting automated and rapid stroke detection to reduce diagnostic errors and improve patient care outcomes.

Keywords—Computed Tomography, Brain Stroke CT Image Dataset, Image Analysis, Artificial Intelligence, Machine Learning, CNN, ResNet, MLP, VGG 16, Noise effect in image for CT.

I. INTRODUCTION

Computerized tomography (CT) has emerged as a crucial diagnostic tool due to developments in cutting-edge medical imaging technology, which has revolutionized the healthcare industry [1][2][3]. By offering quick, painless, and accurate imaging of inside organs, CT scans enhance the diagnosis, monitoring, and treatment of a wide range of medical conditions, including cancer, cardiovascular disease, and neurological problems [4][5]. Its capability to produce volumetric scans in a short time makes CT particularly valuable in emergency environment, oncology, and pre-surgical planning. However, the diagnostic reliability of CT is directly dependent on the quality of the acquired images, making systematic assessment and enhancement of CT image quality a central focus in medical imaging research.

Several factors, including noise, homogeneity, contrast resolution, and spatial resolution, are considered when assessing the quality of CT images [6][7]. Accurate interpretation of anatomical and pathological features is made possible by high-quality CT pictures. On the other hand, diagnostic errors, greater radiation exposure from repeat scans, and diminished confidence in clinical judgements can result from poor-quality images [8][9]. Various factors influence image quality, including scanner hardware design, tube current and voltage environment, detector efficiency, reconstruction algorithms, and post-processing methods. Therefore, a comprehensive understanding of these factors, combined with rigorous image quality assessment, is essential to optimize imaging protocols and maintain consistency across different CT systems in Figure 1 and clinical scenarios.

Fig. 1. CT Scan Images

CT image quality is noise**,** which arises from both quantum fluctuations of X-ray photons and electronic imperfections in detectors and signal acquisition systems[10][11]. The use of low-dose CT protocols, which aim to decrease radiation exposure to patients, is on the rise, yet these protocols amplify quantum noise, which is present throughout the X-ray generating process [12]. Electronic noise, on the other hand, originates from the detection electronics and signal amplification, contributing to random variations in pixel intensities [13][14]. Both types of noise degrade image contrast, obscure fine structural details, and adversely affect both manual interpretation and automated analysis.

The effects of noise in CT images extend beyond mere visual degradation[15][16][17]. Critical for precise diagnosis, treatment planning, and disease monitoring, quantitative data might be compromised by noise. These measurements include tissue density evaluation, lesion segmentation, and radiomic feature extraction [18][19][20]. To mitigate these effects, conventional noise reduction techniques including spatial and frequency-domain filtering, iterative reconstruction, and phantom-based calibration—have been extensively employed. These methods aim to enhance image fidelity while maintaining diagnostic accuracy and minimizing radiation exposure

CT image quality evaluation and improvement have recently been greatly assisted by ML and DL techniques [21][22][23]. CNN and other deep architectures can automatically learn complex noise patterns, perform denoising, and reconstruct high-quality images from low-dose scans. These approaches complement traditional calibration and noise reduction techniques, offering automated, adaptive, and data-driven solutions for image enhancement. Incorporating ML/DL models into traditional approaches allows researchers to enhance CT scans in quantitative and qualitative ways. This leads to more accurate diagnoses, better patient outcomes, and optimized imaging workflows in clinical practice.

A. Motivation with Contribution

The exponential growth of medical imaging, particularly Computed Tomography (CT), has increased the demand for accurate and efficient diagnostic interpretation. However, CT image quality is often compromised by various sources of noise, such as photon fluctuations, detector electronics, and reconstruction algorithms, which obscure anatomical details and degrade diagnostic reliability. Traditional quality assessment methods and simple filtering approaches are often inadequate for handling complex noise patterns while preserving spatial resolution. Research is being driven by the urgent need to develop a comprehensive framework that combines noise characterization, picture enhancement, and advanced learning models. This framework greatly increases the diagnostic utility and quality of CT images in healthcare facilities.

The main contributions of this work on CT image quality analysis and noise effect are as follows:

- Development of a complete workflow for CT image quality analysis, beginning with raw data acquisition and format conversion, followed by preprocessing steps such as resizing, intensity adjustment, noise suppression, and label encoding to ensure standardized and high-quality inputs.
- Data normalization and augmentation approaches, spatial filter-based quantitative noise analysis, picture statistics, and signal-to-noise ratio enhancement and dataset strengthening strategies.
- Research on the effect of noise on the precision of feature extraction and classification in CT images associated with stroke was organized and carried out using several architectural frameworks, including CNN, ResNet, VGG16, and MLP.
- Optimal learning models effectively maintain diagnostic precision in the presence of varying degrees of noise, as demonstrated experimentally by metrics like as PRE, F1, REC and ACC.
- Provision of practical understandings and recommendations for incorporating noise-aware CT image quality analysis into computer-aided diagnostic systems, ensuring

reliable performance in real clinical environments.

B. Significance and Novelity

This study is significant as it presents a robust, scalable, and clinically relevant framework for CT image quality analysis, with a particular focus on stroke-related imaging a critical challenge in diagnostic radiology. Its novelty lies in the development of an end-to-end pipeline that integrates noise characterization, advanced preprocessing, data augmentation, and label standardization, combined with a comprehensive evaluation of multiple learning models, including CNN, ResNet, VGG16, and MLP. This paper presents a comparative analysis under different noise situations, demonstrating the better performance of noise-aware architectures, in contrast to numerous previous research that either concentrate on single-model classification or fail to account for the impact of noise. The inclusion of quantitative noise assessment and enhancement techniques further strengthens feature extraction and classification accuracy, while practical insights for clinical deployment ensure the framework is directly applicable to real-world diagnostic environment. The integration of diverse deep learning approaches with systematic noise handling provides unique insights into model robustness, addressing the critical need for reliable, adaptable, and high-quality CT image analysis in modern healthcare environments.

C. Structure of Paper

The following structure of the paper: Section II provide the Background of image processing in medical sector, Section III Computed Tomography image analysis technique, Section IV Noise characterization and its impact on CT, Section V provide the literature of review in CT image analysis Section VI Research Gaps Section VII discussed the proposed methodology with each phase of this system design, Section VIII evaluate the results of proposed models, comparison, discussion and Application, Limitation and future work, final Section IX presents the findings and recommendations for further research.

II. Background of Image Processing Analysis in Medical Sector

The decision-making and problem-solving capabilities of modern programs rely heavily on image processing algorithms. Disease diagnosis, clinical treatment, and other healthcare services often make use of image processing methods in the medical field. The advancement in medical image processing is increased noticeably. Hence, various types of advance image generation sources are increased. They produce huge sizes of medical images continuously. The following image generation sources play a vital role in medical applications:

- Magnetic Resonance Image (MRI)
- Positron Emission Tomography (PET)
- Computed Tomography (CT)
- Positron Emission Tomography and Computed Tomography (PET-CT)
- Single Photon Emission Computed Tomography (SPECT)
- Ultrasound
- X-ray

1) Magnetic Resonance Image (MRI)

Medical image processing makes use of MRI) to measure the health of inside organs and tissues. Obtaining internal scans, MRI scans employ radio waves and a magnetic field. MRI scans are widely used to identify the difference between the normal individual's body and patient's body MRI scans are used to monitor the blood vessels flow, identify the abnormal tissue, monitor the tumors in the breast, identify the tears in the ligament, function of bones, and monitor the internal organs in the heart, kidney, liver and spleen.

2) Positron Emission Tomography (PET)

PET scans allow doctors to see inside a patient's body by using a high-tech camera and a radioactive substance. A radioactive chemical is in the form of glucose and it is often used during the PET scans to collect the cancer cells from the patient's body. This type of chemical is also called a tracer. The essential role of PET scan is to observe the tissues and organs of the patients who are affected by various health problems such as heart disease, prostate cancer, liver cancer, breast cancer and tuberculosis.

3) Computed Tomography (CT)

CT creates cross-sectional images by capturing X-rays from different angles. In other words, CT scan uses various types of digital geometry processes to take X-ray images from different directions. Images generated from the CT scans are used to image the various types of heart diseases, broken bones, prostate cancers, liver

cancer, breast cancer, internal bleeding, and blood clots and so on

4) Positron Emission Tomography and Computed Tomography (PET-CT)

PET and CT scans are combined to take a complete scan that observes the internal organs and monitor the abnormal anatomic location. This type of scan produces results more effectively than the two scans (PET and CT scans) taken separately. PET-CT scans are widely used to identify cancer in the early stage. Results from this type of scans are used by the doctor to take necessary treatment. Efficient use of PET-CT scan may help to recover people from various cancers and other diseases. PET-CT scans have many medical applications, including the following: regulating cancer levels and their spread, tracking the effectiveness of cancer treatments in real time, studying the heart's blood flow, assessing the impact of a heart attack, and keeping an eye out for abnormal brain conditions, such as the detection of brain disorders, tumors, and bleedings.

5) Single Photon Emission Computed Tomography (SPECT)

A SPECT scan is used to monitor the internal blood flow and functions of internal organs. A combination of CT and a radioactive substance, sometimes known as a tracer, is used in this scan type. PET scans to collect the cancer cells from the patient's body. Radioactive chemical or tracer is injected into the human body via intravenous or IV injections. Tracer or radioactive chemical moves to the internal body.

6) Ultrasound

Ultrasound imaging is one of the medical imaging technologies to observe the swelling, pain and infection in the internal body. The use of high-frequency sound waves allows for the recording of pictures of the inside of the human body using ultrasound imaging. Using ultrasonic imaging technology, which generates high-frequency sound waves, a digital image is formed from the reflected sound. The resultant image generated from the ultrasound technology is used to identify the heart diseases, monitor the human body parts affected after a major heart attack, determine the baby health conditions, monitor the pregnancy status and identify the abnormal situations in the blood vessels.

7) X-ray

X-ray technology is one of the familiar imaging technologies used to take pictures of the internal body. Ionizing radiation is injected from the Xray machines to the human body that shows the body parts by black and white shades. In general, bones have more calcium than other parts of the body.

A. Overview of Computed Tomography

Electrical engineer Sir Godfrey Hounsfield developed the first CT scanner in 1972. It was Hounsfield and Cormack that shared the 1979 Nobel Prize in Physiology or Medicine. A scientist named Allan McLeod Cormack also created a gadget that was similar about the same period. CT rapidly acquired popularity as a medical imaging tool following its introduction. CT scans are flat, three-dimensional models of physical objects. To create these pictures, X-ray photons are transformed from electrical energy, which is basically just moving electrons. The light is then transformed back into electrons after passing through an object and being detected. The density of an item is inversely proportional to its X-ray transmissivity. It is possible to image the components of objects, including humans, using CT scans, which have varying densities.

The CT scanner spins around the item completely, directing X-rays at it from all directions. The density of an object's constituent elements changes as a function of lighting angle, so does the intensity of photons that flow through it. Inconsistencies in successfully transmitted X-ray photon readings rely on a computer processor to build a dataset. The object's densities are subsequently utilized by this dataset to create a three-dimensional replica of it. The dataset is shown on screen or film in a sequence of two-dimensional parts. While there are a number of factors that go into determining picture quality, the two most crucial are image resolution and evaluated contrast.

1) CT Imaging

CT's stellar reputation for radiologic diagnostic accuracy has propelled it to the forefront of medical evaluations. One of the major problems with conventional X-ray imaging is that it can't differentiate between different types of tissues, such as muscles, ligaments, and blood vessels. Computed tomography outperforms the conventional X-ray method by combining multi-angular X-ray scanning with a mathematical theory that reconstructs the object based on its projections. The data collected by an X-ray beam as it moves through a patient's body is largely interpreted by a computer in a CT scan. CT scans make it easy to learn about an object's internal structure,

including its size, shape, internal flaws, and density. It is possible to recreate a picture using X-ray data and the radon and inverse radon transform; this technique is called CT imaging.

2) CT Image Reconstruction

CT makes use of a motorized source of X-rays that are directed at various angles across the patient. On the other side of the X-ray generator sit the specialized digital X-ray detectors that CT scanners use [24]. Detectors transform the X-rays into electrical impulses as they pass through the patient. An analog-to-digital converter takes these electrical signals and turns them into digital information. A digital-to-analog converter may take data from the digital matrix and turn it into little boxes with a range of greyscale to black and white.

3) Major Factors Affecting the Quality of CT Images

The accuracy of CT reconstructions is dependent on a wide range of parameters. Image quality is affected by several important elements, including:

a) Blurring

Appropriate protocol factor values, patient mobility, and other factors might cause CT images to be blurry. Blurring in CT reconstructed pictures might happen when the patient moves about. A number of factors, including an uncooperative patient, breathing, heartbeat, etc., might cause the patient to move. The reconstruction methods are a bit more complex since they need to take into consideration and control the patient's z-direction movement—the degree of blurring in the image is directly related to the patient's momentum. Important reasons of blurring include the following:

- The method of operating the machinery
- The correct values for the procedure factors
- Image blurring as a result of patient motion
- Ct value variation across image pixels for a homogenous material scan
- Poor filter algorithm parameters or some filter algorithms themselves (for noise reduction) haze the picture

b) Field of view (FOV)

The field of vision refers to the area that can be chosen in order to recreate the CT scan. It becomes challenging to detect abnormalities and the quality of the reconstructed CT picture could be diminished if the image is either too large or too small.

a) **Artifacts**

Artefacts are distortions or errors in images that are unconnected to the object being portrayed. Inconsistencies between the expected and displayed CT values are known as artefacts. Metal artefacts, beam hardening, partial volume effects, patient movements, and other similar phenomena are common.

- **Beam hardening:** A patient causes an X-ray beam to harden because its average energy increases as it passes through the body. Cupping is another term for this item. The correct algorithms, together with steps like boosting kvp, lowering slice thickness, pre-filtering X-rays, and, ideally, avoiding regions with high X-ray absorption rates, can help one effectively avoid this.
- **Metal artifact:** Dental fillings, prosthetic limbs, surgical clips, and other metal objects might obstruct portions of projection data, leading to streaking artefacts. By removing the metal material, this artefact can be diminished.
- **Patient motion:** Artefacts of streaking can be generated in the reconstructed image as a result of both voluntary and involuntary motion. In order to prevent this, potential solutions include motion reduction, immobilization, positioning aid, and a reduction in scan time.
- **Software and hardware based artifacts:** Artefacts in CT images may also be produced as a result of inadequate software inputs and inadequate apparatus. Failure of mechanical components, rigidity of the gantry, mechanical assignment, aliasing, detector sampling, staircase, and tube arcing are among the many potential causes of artefacts. Additionally, poor parameterizations during CT image reconstruction lower image quality. If one wants better CT images, they can tweak or optimize a few key parameters in the computed tomography area. The pitch of the reconstructed slice thickness, scan range, patient position, tube current and potential, and detector configuration are all components of the collection of parameters.

c) Visual Noise

Visual noise is any kind of unwanted data that detracts from an image's aesthetic value. There are several potential sources of noise in CT scans. These include differences in voxel attenuation coefficients, mathematical computation mistakes, and faults in acquisition, transmission, and transmission. Disturbance to the visual field has a major influence on image quality, especially for objects with low contrast.

III. Computed Tomography (CT) Image Analysis Techniques

CT scans' great spatial resolution and non-invasive capacity to depict inside structures make them useful in clinical diagnostics. However, raw CT images often contain noise, artifacts, and complex anatomical details that complicate direct analysis. Improving picture quality, extracting useful information, and bolstering automated diagnostic systems are all goals of image analysis. Two main groups of these methods exist: those that rely on more conventional image processing techniques and those that use more sophisticated ML and DL methods:

A. Traditional Image Processing Techniques in CT Image Analysis

Traditional image processing techniques focus on improving image quality and extracting features using deterministic algorithms. Key methods include

1) Noise Reduction:

CT images frequently exhibit noise as a result of modest radiation doses or the scanner. Electromagnetic interference, environmental circumstances, or flaws in the imaging device are a few of the many potential sources of undesired noise in images taken by sensors, cameras, or scanners. Filtering and smoothing are examples of preprocessing techniques that remove noise from images, which improves their quality and allows for more precise analysis.

2) Spatial Filter based Techniques

Denoising CT images with linear filters is a way to enhance diagnostic accuracy and picture quality by reducing noise from CT scans. Each pixel in Figure 2 is averaged with its neighboring pixels using linear filters like median and averaging, which blurs edges but reduces noise. A median filter enhances edge retention and decreases blurring by replacing each individual pixel with the median value of the pixels immediately around it. Linear filters that estimate and remove noise using mathematical models while preserving picture properties include the Gaussian and Wiener filters. The noise type and the intended trade-off between lowering noise and keeping image detail dictate the filter that is most appropriate.

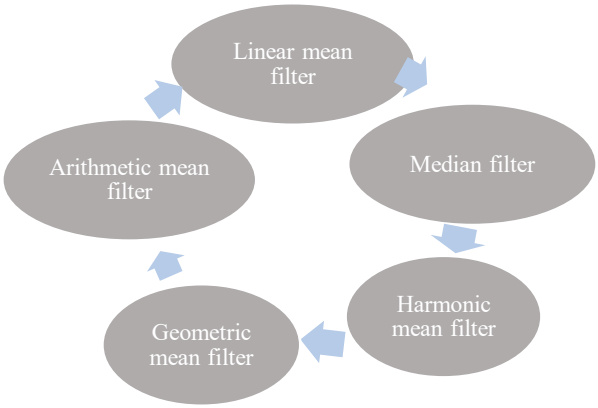

Fig. 2. Spatial Filter based Technique

- **Linear/Mean filters:** Noise reduction, edge sharpening, and illumination imbalance correction are all possible with the help of the linear filter. These filters distort the image's edges and obliterate its fine features. They perform poorly when it comes to reducing signal-dependent noise. The method is implemented by applying a processing kernel correlation filter on the picture. Applying the arithmetic mean filter to the damaged picture yields its average value.
- **Arithmetic Mean Filter:** The central pixel value of the mask is replaced with the arithmetic mean of all the pixel values within the filter window. The local visual discrepancies are simply smoothed down using a mean filter. Reducing noise makes the image smoother, but it also blurs the edges. Equation (1) uses the geometric mean of the Sxy region's pixels to find the restored picture's f value at point (x, y).

$$f(x,y) = \frac{1}{mn}\sum(r,c) \in s_{xy}\, g(r,c) \quad (1)$$

The pixels surrounding s_{xy} are represented by the coordinates r and c, in that order.

- **Geometric Mean Filter:** The difference between an arithmetic mean filter and a geometric mean filter is that the latter uses geometric values. This is the primary difference between the two. A geometric mean filter was used to reconstruct the picture represented by the phrase. In Equation (2), the

phrase stands for a restored image that was processed using a geometric mean filter.

$$\hat{f}(x,y) = \left[\prod_{(r,c)\in s_{xy}} g(r,c)\right]^{\frac{1}{mn}} \quad (2)$$

situations where the word "multiplication" is employed. For every pixel that has been restored, the computation is simply the total of all the pixels in the sub-image region multiplied by $\frac{1}{mn}$.

- **Harmonic Mean Filter:** The harmonic mean approach is beneficial for the preponderance of noises, with the exception of pepper noise. It entails substituting the average grey value of nearby pixels for the grey value of each individual pixel. Several kinds of noise, including Gaussian noise, are well-handled by it.
- **Median Filter:** The median filter, the most famous order-statistic filter in image processing, substitutes the value of a pixel with the median of the intensity levels nearby using Equation (3).

$$f(x,y) = median_{(r,c)\in s_{xy}}\{g(r,c) \quad (3)$$

Where Sxy is a subimage (neighborhood) that is centered on the point (x, y), as previously stated. In determining the median, the pixel's value at (x, y) is being taken into consideration.

3) Wavelet-based Techniques

CT image denoising using wavelet-based filters is a popular technique due to its ability to effectively remove noise Wavelets decompose images into different frequency components, allowing for targeted noise removal and detail preservation. Common wavelet-based filters include thresholding, shrinkage, and wavelet domain filtering

4) Filtering in Frequency Domain

Image sharpness and smoothness can be improved by frequency domain filtering. Low pass filtering, which involves attenuating high frequencies, is used to achieve smoothing. By isolating the high-frequency components and attenuating the low-frequency ones, high pass filtering sharpens the sound. To apply filtering in the frequency domain, one must multiply the image by the filter transfer function. The following is a step-by-step description of frequency domain filtering execution.

B. Machine Learning-Based Techniques in CT

ML enhances CT image analysis by enabling automated recognition and classification of complex patterns. Analytics in medical imaging involve using software to sift through medical imaging data in search of actionable medical information, such as past health issues and current disorders. Developing high-performing medical image analytics systems relies heavily on ML, as seen in Figure 3. This article covers the three main categories of ML: supervised, semi-supervised, and unsupervised:

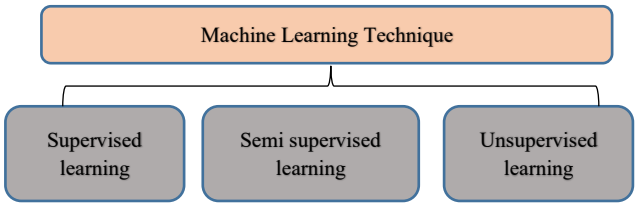

Fig. 3. Machine Learning Technique

1) Supervised Learning

Training DT and NN typically involves supervised learning. The information supplied by the pre-determined classification is crucial to both of these, as indicated earlier [25]. Applications that are able to analyses past data in order to predict future feature events also utilize this learning. Both regression and classification are broad categories that encompass supervised learning activities. This predictive model is constructed by the supervised learning method.

Decision trees: A DT classifier uses a recursive partitioning process to divide the instance space. When the branches of a decision tree come together, they form a root tree, a type of distributed tree that has just one branch (the root) and no branches that branch out.

Linear regression: One of the many regression algorithms, linear regression1 seeks to do just that discover the interdependencies and correlations between the variables. The linear function represented by *Y* in ML models the relationship between a D-dimensional vector containing a continuous scalar dependent variable y (also called a label or target) and one or more explanatory variables (also called features, attributes, dimensions, data point, etc.).

Naive Bayes: Bayesian classification is a statistical method for classification and one of the supervised learning methodologies. Using the establishment of outcome probabilities as a basis, it enables the principled capture of model uncertainty and implies a

probabilistic model. Bayesian classification is primarily designed to address difficulties related to prediction.

Logistic Regression: One way to forecast the probability of an occurrence is using LR, which involves fitting data to a logistic function. LR and other types of regression analysis employ a large number of numerical or categorical variables as predictors.

2) Unsupervised Learning:

The goal of unsupervised learning is to reveal how computers might learn to display input patterns in a way that reflects their statistical structure, rather than the other way around. Unsupervised learning differs from supervised and reinforcement learning in that it relies on the learner's prior biases to decide which aspects of the input structure should be incorporated in the output. In contrast, supervised and reinforcement learning have designated goal outputs or environmental assessments associated with each input.

3) Clustering Based Technique

Clustering methods organize comparable pixels or areas according to their texture, intensity, or other characteristics. Common techniques include:

K-Means Clustering: Clustering, another name for cluster analysis, is an unsupervised ML technique that groups together comparable data points in large datasets without regard to the precise outcome.

DBSCAN (Density-Based Spatial Clustering): Anomalies or irregular lesions in CT scans can be detected with this method since it identifies groups of arbitrary forms.

4) Dimensionality Reduction Techniques

Visualization, noise reduction, and feature extraction are all made easier by dimensionality reduction, which takes high-dimensional picture data and flattens it while keeping important patterns:

Principal Component Analysis (PCA): Extracts the most significant components representing the variance in CT images, aiding in compression and noise suppression.

Autoencoders: Effective denoising and anomaly detection are achieved by using neural network-based models that learn compact representations of CT images. These models restore normal patterns and identify deviations, making them ideal for these tasks.

a) Semi-Supervised Learning

A subset of ML techniques is semi-supervised learning (SSL). The dataset is intermediate between supervised and unsupervised learning because of its incomplete labelling [26]. Obtaining completely labelled datasets for CT image analysis can be a lengthy, laborious, and costly process that necessitates the services of trained radiologists. By utilizing the vast quantities of unlabeled data, semi-supervised approaches enhance model performance while decreasing reliance on annotated images. Resolving issues with both supervised and unsupervised learning is central to SSL's mission. The time and data needed to train supervised learning to classify test data is substantial, despite the efficiency of the method. Unsupervised learning, in contrast, uses clustering or the maximum likelihood approach to group data points according to their similarities without labelled data.

C. Deep Learning-Based Techniques in CT

DL is a subset of a larger class of ML techniques that use representation learning and are based on ANNs. A computational architecture is provided by deep learning, which learns from data by merging many processing layers, such as input, hidden, and output layers [27]. The three most popular deep learning algorithms are LSTM-RNN, MLP, and CNN, or ConvNet.

CNN: The CNN incorporates pooling, convolutional, and fully linked layers, which enhance the conventional ANN architecture.

MLP: A multilayer perceptron (MLP) is another name for the feed-forward ANN. A typical MLP network consists of three primary layers: input, hidden, and output.

LSTM-RNN: LSTM is an artificial architecture used in DL. When compared to traditional feed-forward neural networks, LSTMs feature feedback linkages.

ANN: The architecture and operation of the human brain serve as inspiration for ANNs. Complex non-linear mappings between inputs and outputs can be learnt by the neurones that comprise them. Since ANNs can pick up on finer patterns in high-dimensional imaging data, they find extensive application in CT image processing for tasks like segmentation, feature extraction, and classification.

IV. Noise Characterization and Its Impact on Computed tomography (CT) Image Quality

CT image quality is critically influenced by various types of noise, which can obscure anatomical structures, reduce diagnostic accuracy, and affect quantitative measurements. Understanding noise sources, their characteristics, and mitigation strategies is essential for reliable image analysis and subsequent clinical decision-making. This section presents the types of noise in CT imaging, methods for measurement, and techniques for noise reduction and calibration

A. Noise in CT Images

The delicate tissues of the human body are distinguished using CT's high contrast sensitivity. The capacity to perceive low-contrast structures can be impaired when noise is present. Accurate denoising of CT scans necessitates familiarity with both the specific kinds of source noise and the characteristics of generic noise

B. Sources of Noise in CT Imaging

The physics of X-ray capture, faulty scanner electronics, and inefficient reconstruction methods are only a few of the sources of noise in computed tomography (CT) pictures. There are several primary sources including:

1) Quantum (Photon) Noise

The most common kind of image degradation in CT scans is known as quantum (photon) noise, which results from the randomness of the X-ray photons observed during the acquisition process. Because X-rays are emitted and absorbed according to probabilistic (Poisson) statistics, the signal collected by the detector fluctuates around a mean value, producing grainy variations in pixel intensity. Figure 4 displays the different gantry types and the semiconductor materials employed by the various systems [28].

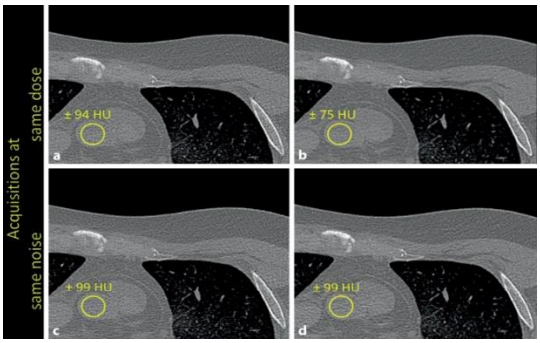

Fig. 4. CT Image in Effected Noise

This type of noise becomes particularly pronounced in low-dose CT scans, where reducing the radiation exposure inherently decreases the photon count.

2) Electronic Noise

An x-ray detecting device can lessen electrical noise. Radioactive particles and beam strengthening. The detectors used in modern CT systems are solid-state devices [29]. The x-rays are transformed into visible light by the radiation-sensitive solid-state components that are used in every detector cell. Common examples of these materials include gadolinium oxide, cadmium tungstate, and gadolinium oxysulfide.

3) Reconstruction Algorithm Effects

Traditional filtered back projection (FBP) methods for reconstructing CT images usually result in increased picture noise despite decreased radiation dosage [30]. But new iterative reconstruction (IR) algorithms outperform their predecessors significantly when exposed to modest levels of radiation when it comes to noise. There is no clinical agreement on what constitutes a "acceptable" level of noise, even though CT screening for benign lesions can tolerate some noise in order to decrease the radiation dosage. The most optimal method would involve creating images with a tolerable amount of noise using infrared algorithms and low-dose parameters.

C. Methods for Noise Measurement

Quantifying CT image noise accurately is crucial for assessing picture quality, refining imaging protocols, and directing post-processing methods. Noise in CT images is typically quantified using both spatial and frequency-domain approaches, as well as signal-to-noise-based metrics.

1) Signal-to-noise and contrast-to-noise ratios

Commonly employed in signal processing are the SNR and the CNR, both of which measure image quality. The proportion of the average signal strength to the noise standard deviation is the definition of ROI and the criteria for meeting specifications. Although there are numerous different ways to define SNR, the most popular one is given by Equation (4):

$$CNR = \frac{|Mean_{Region1} - Mean_{Region2}|}{standard\ deviation\ of\ noise} \quad (4)$$

Equation (5) defines the signal-to-noise ratio, or SNR, as the ratio of the two:

$$SNR = \frac{Mean\ signal\ in\ ROI}{standard\ deviation\ of\ noise} \quad (5)$$

An improved SNR improves the reliability of computer analyses and the quality of the images produced by them.

2) Noise Power Spectrum

The NPS is a spatial frequency-dependent description of a system's noise response. Equation (6) is used to evaluate the NPS over N ROIs:

$$NPS = \frac{1}{N}\sum_{i=1}^{N} |F[I_i(x,y,z) - \overline{I_i}|^2 \frac{\Delta_x\Delta_y\Delta_z}{N_xN_yN_z} \quad (6)$$

The variables Ii, which represents the average signal strength in each voxel in ROI i, F, which stands for the Fourier transform operator, $\Delta_x\Delta_y\Delta_z$, which denote the x, y, and z dimensions of the voxels, and $N_xN_yN_z$, which denote the dimensions of each ROI in voxels, are all involved.

3) Root Mean Square Error

A voxel's root-mean-squared signal intensity difference (RMSE) between its reference and test images is equal to the average of all squared signal intensity differences between the two sets of data. This formula is described by Equation (7):

$$RMSE = \sqrt{\frac{1}{MN}\sum_{i=1}^{M}\sum_{j=1}^{N}(x(i,j) - y(i,j)^2} \quad (7)$$

where x (i, j) is the reference image's grey level for a given voxel and y (i, j) is the test image's grey level for the same voxel. M is the sum of all horizontal voxels and N is the sum of all vertical voxels.

Noise Reduction and Calibration in CT Imaging

Table I provides an overview of key noise reduction and calibration techniques in CT imaging. These methods improve image quality by minimizing noise while maintaining diagnostic accuracy and patient safety.

TABLE II. OVERVIEW OF KEY TECHNIQUE IN NOISE REDUCTION IN CT IMAGE ANALYSIS

Technique	Description	Primary Purpose
Acquisition Parameter Optimization	Adjusting tube current (mA), voltage (kVp), rotation time, and pitch to balance image noise and radiation dose.	Improves image quality while minimizing patient exposure.
Iterative Reconstruction Algorithms	Advanced reconstruction methods (e.g., adaptive statistical iterative reconstruction, model-based IR) that reduce noise	Produces smoother images with better detail at lower doses.
Detector Calibration	Routine calibration of detector gain, offset, and uniformity to ensure consistent performance across detector elements.	Minimizes electronic and fixed-pattern noise.
Scatter Correction	Hardware or software techniques that reduce scattered radiation reaching the detector.	Enhances contrast and reduces streak-like noise.
Beam Hardening Compensation	X-ray beam energy correction algorithms that account for the transition of the beam through dense tissues.	Reduces streak artifacts and non-uniform shading.
Post-Processing Filters	Adaptive, anisotropic, or deep-learning–based filters applied to smooth noise while retaining structural detail.	Enhances image appearance without degrading resolution.
Protocol Standardization	Harmonizing acquisition and reconstruction environment across scanners and operators.	Improves reproducibility of image quality and noise levels.

V. Literature of Review

This section provides a literature overview on AI methods for efficient and accurate analysis of CT picture quality, with an emphasis on methods for detecting strokes. Table II summarizes the key studies discussed below:

Jiang et al. (2025) A state-of-the-art detection framework that can identify CT flaws by their structural features. The model employs an EPCB to acquire edge information, particularly at defect borders, in order to enhance localization and classification. To further improve the detection of intricate and nuanced defect patterns, a new backbone called the edge-prior net (EP-Net) was also introduced. At many different spatial scales, this network contains features. During inference, the multi-branch structure is reduced to its single-branch counterpart, allowing for quicker detection without influencing accuracy. Experimental results demonstrate that Defect R-CNN achieves an average accuracy (AP) greater than 0.9 for all types of defects in a CT dataset composed of radioactive graphite components from an HTGR. In comparison to popular approaches such as Faster R-CNN, Mask R-CNN, Efficient Net, RT-DETR, and YOLOv11, the model achieves better results with bounding box (mAP-bbox) and segmentation mask (mAP-segm) scores of 0.983 and 0.956, respectively. Because it strikes a good mix between efficiency and accuracy, the inference pace of 76.2 FPS is ideal [31].

Shim, Lee and Kim (2025) Minimizing radiation exposure during CT imaging is of the utmost importance, especially for routine and repeat exams. Two DLIR algorithms, GE TrueFidelity (TF) and Philips Precise Image (PI), were evaluated in an 80 kVp low-dose CT scenario using the AAPM CIRS-610 phantom, which simulates clinical imaging settings, to ensure that diagnostic quality is maintained during DLIR low-dose collection. Under low-dose circumstances, the phantom's linearity, high-resolution, and artefact modules were scanned with GE Revolution and Philips CT 5300 CT scanners. This evaluation was based on eight quantitative variables: SNR, CNR, nRMSE, PSNR, SSIM, FSIM, UQI, GMSD, and gradient magnitude. Reconstruction of the photos was done using the following five DLIR presets: TF (Middle, High), PI (Smoother, Standard, Sharper). In terms of SNR, TF-High outperformed PI-Smoother (115.0-118.0 across modules), obtained a higher PSNR, and had the lowest GMSD. These results suggest that the structure in low-dose images was more effectively preserved. The dominant solution was PI-Sharper in terms of gradient magnitude. The best mix of structure integrity and noise suppression was provided by TF-High for low-dose CT, whereas PI-Sharper excelled at enhancing fine details [32]

Zhou et al. (2024) application of DL-based image reconstruction and noise reduction algorithms, or DLIR, has increased in clinical computed tomography (CT). This method is employed to evaluate the spatial resolution of a DCNN that is based on ResNet and has been trained on patient images. In one patient's case, the lower left lobe of the liver was implanted with lesions that had variable degrees of contrast (−500, −100, −50, −20, −10 HU). The dosage levels of 50%, 25%, and 12.5% were all simulated. Each lesion and dose condition were associated with a minimum of 600 noise realizations. Three distinct intensity environments—DCNN-weak, DCNN-medium, and DCNN-strong were used to train deep convolutional neural networks (DCNNs), iterative reconstruction (IR), and the original filtered-back projection (FBP) on all of the noisy realizations. Decreasing the number of lesion pictures from the total number of images by first locating the noise in each dose condition and lesion. The 50% in-plane and z-axis MTFs decline from 92.1% to 76.3% and 95.5%, respectively, under varied contrast and dosage settings, when the dose level is dropped from 50% to 12.5% normal dose utilizing FBP [33].

Li et al. (2024) One of the most cutting-edge imaging methods is CT. Adaptive assessment of blurring effects caused by insufficient sampling of the LR X-Ray detector using a DL network (SRECT-Net). Once the scanning technique is set for a CT machine, the blur effect pretty consistent. This finding provides the impetus for the suggested approaches, which can be pre-trained using plenty of simulated datasets, fine-tuned with a single sample, and finally provide a machine-specific SR model. Compare the performance of the suggested SRECT against that of existing DL-based CT SR techniques using SR CT imaging on a Catphan700 phantom and a ham. The results show that the proposed SRECT is more effective than current state-of-the-art CT SR reconstruction methods, which might be useful for improving CT resolution [34].

Parameswari et al. (2024) CT scans one at a time and compare three different CNN models to one thousand CT scans of the heart and blood vessels, both healthy and with calcium deposits. Three types of CT-image data are used in experimental test: original CAC-

score CT, cardiac-segmented, and cardiac-cropped. The rib cage as a whole is included in the first set, while the heart region is excluded from the second two sets. Using Inception ResnetV2, VGG, and Resnet50, the exploratory test for calculating the incidence of calcium in a CT-picture had the highest accuracy rate of 98.52% [35].

Bos et al. (2024) CT images. The 152 adult head CT scans that were included were acquired between March and April 2021 from three separate CT scanners using various methods. From 77 to 75 years old, the participants' ages ranged from an average of 69.4 ± 18.3 years. A deep learning-based method was employed for post-processing following the CT image reconstruction utilizing FBP and IR. Depending on the technique, postprocessing greatly decreased noise in FBP-reconstructed images (by as much as 15.4% reduction), which improved the signal-to-noise ratio by as much as 19.7%. These results seemed to be protocol or site dependent. There was no discernible improvement in picture quality across the board for any reconstruction or post-processing, according to subjective evaluations. Reliability between raters was poor, and preferences differed. Using deep learning-based denoising software yielded superior objective images in regular head CT scans compared to FBP. One of the methods was the sole one that varied substantially from IR. Subjective assessments did not show a substantial therapeutic impact in terms of improved subjective image quality due to the low noise levels of full-dose images [36].

S P et al. (2024) preservation of information and the restoration of images tainted by noise rely heavily on CT medical images. Although the CNN was effective in removing the noise, the performance cost us clarity and the ability to preserve small features, which made the CT scans unusable. Ischaemic stroke patients' brain CT images can be segmented and classified more accurately with the application of MA-CNN, an improved noise removal method. One way to measure how well an MA-CNN works is by looking at its PSNR. The results show that the proposed model outperforms current denoiser approaches in terms of PSNR and ensures the preservation of high-quality pictures [37].

Abubaker, Mohamed and Abuzaid, 2023, Processing of images from computed tomography scans. One model, CTcov_model, is designed to process images from CT scans and is based on the previous model; another, Xcov_model, uses CNN and DL to process images from CXRs. In order to generate a heat map showing the predicted spread of the disease, the Grad-Cam algorithm provided support for both models. The nine thousand images that made up the dataset were split evenly across three categories for CT and x-ray imaging. With the help of DA technology, trained on 80% of these photos and tested on 20%. With an F1-Score of 98%, the Xcov_model stood out among the models that were developed and tested on the Google Collaboratory platform using Python [38].

Mahmoodian et al. (2023) uutilizing computed tomography (CT) pictures that segment four distinct tissue structures, the lungs, the tumors, the ablated tissues, and the surrounding healthy tissue MWA therapy is a famous method for targeting and eliminating tumors in the lung. Use the IoU to quantify the suggested method's efficacy. Background, lung, ablated, and tumor tissues all have the highest average IoU values of 0.99, 0.98, 0.77, and 0.54, respectively, as shown by the approach. The results demonstrate that, even with the limited dataset, DL approaches when combined outperform individual base-learner models for all four kinds of tissue. Importance in medicine Determining when all tumor tissue has been totally eliminated is a crucial issue with tumor ablation treatment [39].

Zeng et al. (2022) Using a noise-generating mechanism, Un-SinoNet trains an unsupervised DL network, offering a unique method to low-dose CT sinogram recovery. Training network using unlabeled low-dose CT scans. While learning the right gradient for low-dose CT sinograms unsupervised, Un-SinoNet should take into account the prior measurement features and statistical fluctuations in the CT noise-generation process using a maximum a posteriori probability (MAP) framework. Network training can be made more effective by using the gradient information from both the labelled high-dose CT sinogram and the unlabeled CT sinogram. To turn the proposed Un-SinoNet into a semi-supervised DL network (Semi-SinoNet) that integrates the conventional and MAP goal functions, another option is to employ a small number of low-dose/high-dose sinogram pairs. Executed the expected Un-SinoNet and Semi-SinoNet using the LUNGMAN phantom and the Mayo Clinic patient simulation datasets. This research outperforms competing methods in terms of picture resolution and noise reduction using both methodologies [40].

Inkinen et al. (2022) standard deviation of pixel values from uniform picture portions is a popular method for determining CT image noise. Experimented

with DCNN CNN architecture for direct noise image estimation and UNet-CNN for denoised picture subtraction utilizing supervised and unsupervised noise2noise training methods. Took a look at the background noise using local SD maps and CNN architectures in 3D and 2D. The DL-model was trained using data collected from a nine-scan, three-repetition anthropomorphic phantom CT imaging dataset. The most effective method for direct SD estimation using 3D-CNN was demonstrated on a phantom dataset, with MSE = 6.3HU and MAPE = 15.5%. Even in clinical contexts when ground truth data is unavailable, the noise2noise approach could still be useful. It is possible to characterize image quality more thoroughly by combining noise estimation with tissue segmentation [41].

Recent research in computed tomography has increasingly centered on the application of ML to optimize image quality, particularly through effective noise suppression while safeguarding diagnostically important structures. A range of DL reconstruction strategies has emerged, including convolutional and morphology-aware networks capable of producing cleaner, high-contrast images from low-dose acquisitions. Super-resolution approaches have been proposed to counter detector blur and sharpen subtle textures, while unsupervised and semi-supervised models allow denoising and sinogram restoration in scenarios with limited or unlabeled data. Other investigations emphasize post-processing pipelines that enhance standard reconstructions or integrate noise removal with tasks such as lesion segmentation and anatomical classification, supporting more accurate and streamlined diagnostic workflows. Collectively, these studies indicate a clear trend toward solutions that balance noise reduction, spatial resolution, and computational efficiency, with increasing attention to generalizability across scanners, interpretability of network outputs, and real-time feasibility for clinical deployment. The increasing amount of research demonstrates how machine learning has the power to revolutionize CT imaging, make low-dose procedures safer, and improve the accuracy of quantitative evaluations in a wide range of healthcare environment.

TABLE III. COMPARATIVE ANALYSIS OF RECENT STUDIES ON COMPUTED TOMOGRAPHY IMAGE QUALITY AND NOISE REDUCTION USING MACHINE LEARNING.

Author(s), Year	Dataset	Methodology	Key Findings	Noise Reduction / Image Quality	Limitations	Future Work
Jiang et al. (2025)	CT of nuclear graphite components (HTGR)	Defect R-CNN with Edge-Prior Conv. Block (EPCB) & EP-Net backbone; multi-branch → single branch at inference	AP > 0.9 for all defects; mAP-bbox 0.983, mAP-segm 0.956; 76.2 FPS; outperforms Faster/Mask R-CNN, YOLOv11	Focus on structure & localization (not explicit denoising)	Only graphite dataset; industrial context	Extend to other CT materials; combine with real-time inspection
Shim, Lee & Kim (2025)	AAPM CIRS-610 phantom; Philips CT5300 & GE Revolution, 80 kVp	Deep-Learning Image Reconstruction (DLIR): Philips Precise Image (PI) & GE TrueFidelity (TF) – 5 presets	TF-High SNR 115–118 (+54–57% vs PI-Smoother); best PSNR & lowest GMSD; PI-Sharper gives highest gradients	optimal balance noise suppression	Phantom only; vendor-specific	Validate in clinical scans; cross-vendor DLIR
Zhou et al. (2024)	Patient liver CT; lesions inserted at contrasts −500→−10 HU; 600 noise	ResNet-DCNN vs FBP & IR; assessed MTF spatial resolution	DCNN preserved resolution better than FBP/IR as dose ↓	denoising with spatial-res analysis	Simulated lesions, not natural pathology	Apply to real lesions; improve ultra-low-dose

	realizations; 3 dose levels					
Li et al. (2024)	Catphan700 phantom & ham specimen	SRECT-Net for super-resolution to counter detector blur	Outperforms other SR CT; high-res recon from LR detector	Resolution ↑ (not direct noise)	Phantom only; clinical value unclear	Test on patient CT; embed in reconstruction
Parameswari et al. (2024)	1200 cardiovascular CT scans	Inception-ResNetV2, VGG, ResNet50 on original, segmented & cropped CT	98.52% accuracy for coronary calcium; cropped best	Not aimed at noise; classification	One dataset, limited pathologies	Larger & noisy datasets; robustness studies
Bos et al. (2024)	152 adult head CTs from 3 scanners	FBP, IR, DL post-processing (PS)	DL post-processing cut FBP noise ≤15.4%, SNR ↑19.7%; subjective gain small	Yes – objective noise ↓	Only modest subjective benefit; protocol-specific	Assess with dose-reduction; optimize for user perception
S P et al. (2024)	Brain CT (ischemic stroke)	Morphology-Aware CNN (MA-CNN) for denoising	Higher PSNR vs other denoisers; fine detail preserved	Explicit noise reduction & detail retention	Not tested on big datasets or full pipeline	Integrate with segmentation/classification; real-time
Abubaker et al. (2023)	9000 CT & CXR (3 classes)	CNNs (Xcov_model, CTcov_model) + Grad-CAM	F1 ≈ 98% (CXR); CTcov effective for CT	No – classification only	No CT noise analysis; no baseline compares	Add quality/noise metrics; extend to detection
Mahmoodian et al. (2023)	Lung CT for microwave-ablation therapy	Ensemble of DL models for segmentation (lung, tumor, ablated)	IoU: 0.99 background, 0.98 lung, 0.77 ablated, 0.54 tumor	Focus on segmentation; not denoising	Tumor IoU moderate; small data	Expand data; integrate dose & noise handling
Zeng et al. (2022)	LUNGMAN phantom; simulated Mayo sinograms	Unsupervised Un-SinoNet & Semi-SinoNet for sinogram recovery (MAP)	Better resolution & noise removal vs baselines	Yes – low-dose sinogram denoising	Mostly phantom/sim data	Apply to patient sinograms; refine MAP prior

VI. Research Gaps

Current DL models have made great strides in stroke detection, however there are still several gaps that are directly related to the study's goals and objectives. This void encompasses

- **Data Limitations:** The capacity of many current models to generalize across varied populations and therapeutic contexts is compromised due to their dependence on tiny and frequently homogeneous datasets. The model's generalizability to different types of strokes and imaging quality is enhanced with the addition of a larger and more diverse dataset. This dataset comprises 9,900 photos for testing and 2,501 images for training/validation, thus reducing data constraints. In order to guarantee accurate

stroke identification across different clinical environment and imaging situations, this work tries to increase the model's generalizability by increasing the dataset.

- **Model Complexity and Efficiency:** In real-time clinical situations, complicated models like ResNet50 may not be viable due to their high computing costs. Through hyperparameter tweaking, this study seeks to optimize the CNN architecture for real-time stroke detection by achieving maximum efficiency and minimizing computing complexity without sacrificing accuracy. In comparison to more complicated models as in, the suggested model achieves great performance with substantially fewer operations by optimizing its architectural design, thus reducing computing complexity. The model's exterior accuracy (89.73%) lags behind state-of-the-art standards, but its practicality for real-time application is guaranteed by its reduced design (20 M parameters), fulfilling a major clinical necessity. An important obstacle to the use of AI in stroke care has been eliminated by these optimizations, which allow for real-time inference on conventional clinical hardware.
- **Segmentation and Localization:** Accurately segmenting and localizing ischaemic lesions is still a difficulty, even though stroke detection accuracy is getting better. In order to make informed clinical decisions, it is essential to accurately segment the ischaemic core. In order to achieve very accurate ischaemic stroke localization, this project concentrate on building a CNN model that is specifically designed for stroke detection in CT images.
- **Interpretability and Clinical Trust:** Clinical practice has been slow to embrace deep learning models due to their lack of transparency. This study intends to boost clinician trust by making the CNN model more interpretable and by providing clear visual explanations for stroke predictions using explainability approaches.
- **Real-World Validation:** Validation in real clinical environments is frequently absent, despite the fact that current models have demonstrated promise in controlled environments. The purpose of this study is to evaluate the CNN model using crucial metrics such as accuracy, precision, recall, F1-score, and AUC-ROC in order to ensure its reliability and effectiveness for real clinical usage.

VII. Methodology

CT images to assess their clarity, contrast, and diagnostic accuracy while identifying and quantifying the impact of noise. Noise arising from photon statistics, electronic components, or reconstruction algorithms can degrade spatial resolution and obscure anatomical, affecting clinical interpretation. Careful analysis of image quality metrics, along with noise measurement and reduction strategies, ensures reliable visualization and enhances the diagnostic value of CT imaging The proposed approach for Computed Tomography (CT) image analysis in brain stroke detection follows a comprehensive pipeline, as depicted in Figure 5. A curated dataset of CT images of the brain from strokes was first assembled in DICOM format and then converted to NIfTI format to make it accessible across all software platforms. Images were preprocessed to ensure they were ready for learning. This included scaling them to a fixed spatial resolution, pixel-intensity transforming them to make soft tissue contrast more noticeable, converting colours as needed, applying spatial filters to remove noise, and label encoding them so they could be associated with their respective diagnostic categories. A range of data augmentation procedures were employed to rectify class imbalance and increase dataset diversity. These techniques included rotating, horizontal and vertical flipping, scaling, and random cropping. Following this, image normalization was applied to stabilize pixel distributions and speed up convergence during training. Properly sized training, validation, and testing subsets were created from the processed dataset, ensuring that each split had an adequate representation of each class. After that, various learning architectures such as ResNet, MLP, and CNN were used to automatically classify regions affected by stroke by extracting spatial and textural features from the preprocessed CT images. The model's hyperparameters, such as learning rate, batch size, and dropout rate, were optimized with the help of the validation set. Methods for early pausing were used to avoid overfitting. Lastly, during testing, verified the trained models' F1-score, recall, precision, and accuracy on fresh data. Efforts paid off, and now know which design has the best chance of aiding

clinicians in making decisions about CT-based stroke analyses.

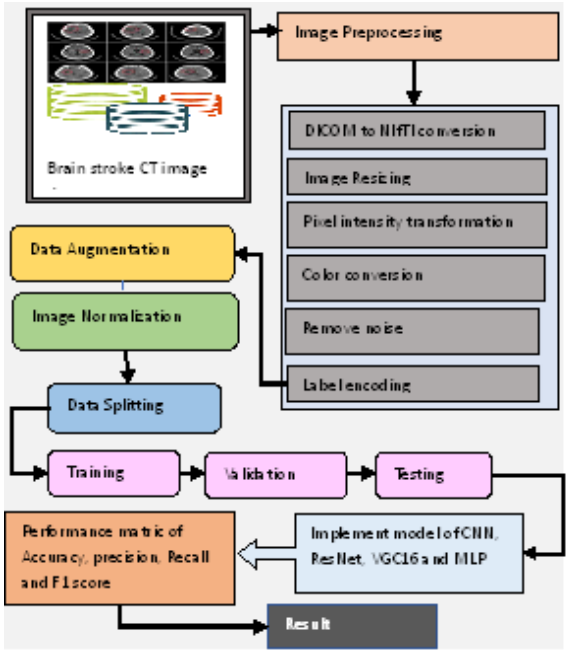

Fig. 5. Flowchart for computed tomography image analysis using machine learning

A. Data Collection

"Normal" and "Stroke" are the two types of brain CT images that make up the dataset used for this research. There are a variety of sizes and resolutions among the 2501 photos in the dataset, which includes 1551 normal and 950 stroke photographs. Brain scans showing ischaemic regions or haemorrhages are placed in the "Stroke" category, whereas those showing normal brain structure are placed in the "Normal" category. Image show most features have low variation except one with high values, highlighting its relevance for computed tomography image some of the visualizations are given below:

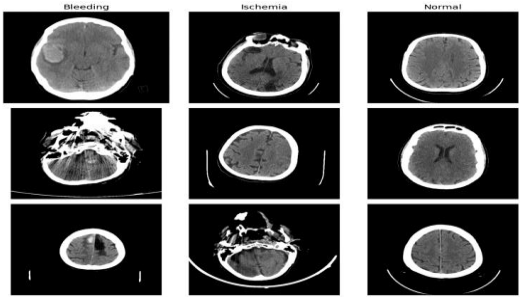

Fig. 6. Sample image of stroke brain CT dataset

Sample images from stroke brain CT dataset showing three categories of brain conditions across nine axial CT scan slices in Figure 6. The dataset comprises three distinct classes bleeding displaying hyperdense regions indicative of acute hemorrhage, ischemia showing hypodense areas characteristic of infarction, and normal presenting typical brain parenchymal density patterns. Each row represents different anatomical levels of the brain, demonstrating the diverse presentation of pathological findings across various cranial sections. The images are presented in standard grayscale CT format with bone window environment, providing clear visualization of intracranial structures and pathological changes essential for automated stroke classification systems.

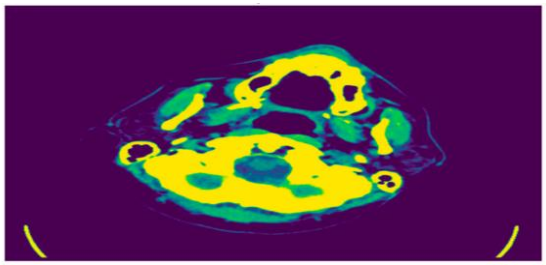

Fig. 7. Heatmap of Predicted Stroke Image

Heat map visualization of activation regions in brain CT scan showing automated feature extraction and attention mechanisms in Figure 7. The color-coded overlay displays varying intensity levels of model activation, with yellow regions indicating highest activation areas, green showing moderate activation, and blue representing lower activation zones against the purple background. Stroke classification using this thermal mapping method reveals the convolutional neural network's focus areas, drawing attention to the most diagnostically important anatomical features and pathological areas that aid in the automated decision-making process for differentiating between ischaemic, bleeding, and normal brain conditions.

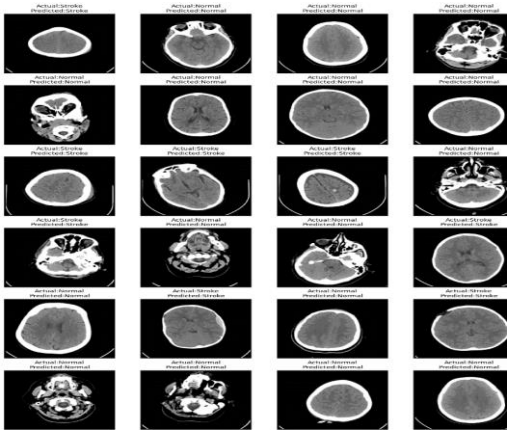

Fig. 8. Actual and predicted normal images

Classification results matrix displaying model predictions versus ground truth labels for stroke brain CT dataset validation in Figure 8. The 6×4 grid presents 24 representative test cases with actual clinical diagnoses (ground truth) labeled above each image and corresponding model predictions shown below. The dataset encompasses three primary categories: stroke (hemorrhagic and ischemic), normal brain anatomy, and various pathological conditions. Each CT scan slice demonstrates the algorithm's performance in automated classification, revealing both successful predictions and potential misclassification cases.

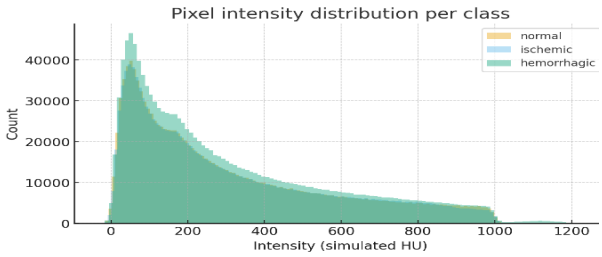

Fig. 9. Pixel intensity distribution per class

Pixel intensity distribution analysis across three stroke classification categories in brain CT dataset in Figure 9. The histogram displays the frequency distribution of Hounsfield Unit (HU) values for normal (orange), ischemic (blue), and hemorrhagic (green) brain tissue classes. The hemorrhagic class exhibits the highest pixel count concentration in the lower intensity range (0-200 HU), indicating hypodense characteristics typical of acute bleeding. Normal and ischemic tissue show overlapping distributions with peaks around 100-150 HU, representing standard brain parenchymal density. The exponential decay pattern across all classes demonstrates the predominance of lower-intensity pixels in CT brain imaging, with hemorrhagic regions.

B. Image Preprocessing

The preprocessing pipeline includes DICOM to NIfTI conversion for format standardization, image resizing to uniform dimensions, pixel intensity transformation using Hounsfield Units with windowing, color conversion to RGB format, noise removal via filtering techniques, and label encoding for categorical classifications. Data augmentation enhances dataset diversity through rotations and transformations, while image normalization standardizes pixel ranges. Data splitting creates stratified training, validation, and testing subsets ensuring balanced distributions. Key steps in data preprocessing include:

- **DICOM to NIfTI conversion:** The control CT images were converted from their native DICOM format to a three-dimensional non-proprietary NIfTI-1 file format. This conversion made it easier to preprocess images with SPM8 afterward, since the latter uses the NIfTI-1 file format for its image data.
- **Image Resizing:** Using bilinear interpolation, all of the photos were scaled down to a consistent 256 × 256-pixel dimension.
- **Pixel intensity transformation:** Intensities of the pixels in the CT scans. The Hounsfield unit (HU) was used to measure the pixel intensities. Through the utilization of the formula HU + 1000, the HU range of -1000 to -100 was elevated to 0-900.
- **Color conversion:** The term "colour conversion" refers to the process of changing an image's colour space from one standard to another. It facilitates the separation of colour, saturation, and brightness, which in turn facilitates picture enhancement, segmentation, and analysis. In CT image visualization, grayscale conversion or applying specific color maps improves contrast and highlights structures or lesions more clearly.
- **Remove noise:** Denoising, or noise removal, is a technique for improving images by minimizing distracting noise while preserving finer details. The Gaussian filter is a popular tool for noise reduction because it flattens images by averaging the values of nearby pixels using a weighted Gaussian function. This helps to reduce high-frequency noise while keeping the general structures of the images intact.
- **Label encoding:** ML models can make use of numerical representations of category labels (such as text-based class names) through a process known as label encoding. A brain stroke CT dataset, for instance, could have the labels "normal," "ischaemic," and "hemorrhagic" recorded as 0, 1, and 2, respectively, for each of these distinct categories. This method is simple and efficient for algorithms that can naturally interpret ordinal values.

C. Data Augmentation

Data augmentation involves "transforming" visual data for training purposes in order to increase the amount of data. A number of transformations are possible with images, including rotation, flipping, horizontal shifting, scaling, distortion, brightness/contrast adjustments, and noise addition [42]. Through data augmentation, the number of photos rose by a factor of nine. The majority of computed tomography (CT) scans involve the patient lying face down, however certain facilities arrange their patients so that their left side, where their hearts are located is positioned precisely in the center of the FOV. In such a situation, the body can end up rotating around 10 degrees due to the bed's curvature. In each image, the heart was rotated by -10° and +10° to mimic this effect, bringing its tilt into alignment with what was shown in the real CT scan. Results from efforts to make contrast-enhanced CT images more resistant to pixel value changes caused by the fact that contrast agent density varies from case to case are shown in Figure 10.

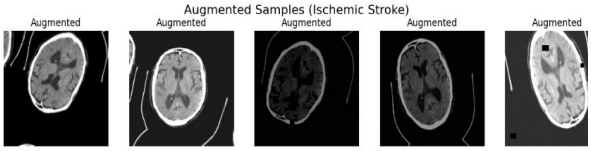

Fig. 10. Augmented Sample Image

All of these methods included rotating, adjusting the height and breadth, shearing, zooming, and horizontally flipping. To make the model more resistant to unknown input, it is necessary to introduce variability into the training data.

- **Rotation:** The following is the rotation matrix for an angle θ:

$$R(\theta) = \begin{bmatrix} \cos\theta & -sin\theta \\ \sin\theta & \cos\theta \end{bmatrix}$$

- Translation (shifting): so that δ_x and δ_y represent a change in the x and y axes, respectively.

$$T(\delta_x, \delta_y) = \begin{matrix} 1 & 0 & \delta_x \\ 0 & 1 & \delta_y \\ 0 & 0 & 1 \end{matrix}$$

- Scaling (Zooming): To apply an S-fold scaling to a picture, the scaling matrix is

$$S(s) = \begin{bmatrix} s & 0 \\ 0 & s \end{bmatrix}$$

D. Image Normalization

The values of the pixels were scaled down to the interval [0, 1] by dividing them by 255. It alters the intensity value range of the pixels and transforms an input picture into a visually more recognizable format. When it comes to grade descent, it's quicker and steadier. The model's convergence during training is accelerated by this normalization phase, which scales the input characteristics to a standard range.

E. Data Splitting

The dataset was divided into 3 sections, as shown in Figure 11, with training comprising 80%, validation 10%, and testing 10%. This division utilized a substantial portion of the data to train the model.

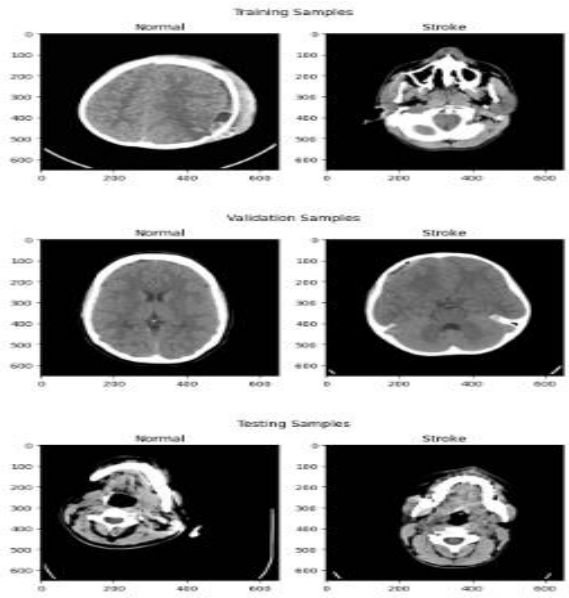

Fig. 11. Data Splitting Sample Training Validation and Testing

Although objective assessments of its efficacy are provided by distinct validation and test instances.

F. Proposed Models

This section provides a theoretical overview of the ML algorithms that were utilized in this investigation.

1) Convolutional Neural Network (CNN)

CNNs have quickly become the gold standard of image classification methods due to their exceptional performance in applications such as object detection, activity recognition, segmentation, and illness diagnosis. CNNs' capacity to learn and extract features autonomously, without any prior knowledge or human involvement, gives them the advantage of being able to differentiate complicated picture shapes [43]. Figure 12

displays the several layers utilized by CNN architectures, such as convolutional, pooling, and fully connected layers, that enable them to learn and extract visual data independently. The following formula is utilized to ascertain the values of successive feature maps; here, h represents the kernel and f represents the picture input. In Equation (8), the row and column indexes of the result matrix are represented by *m* and *n*, respectively.

$$G[m,n] = f(x)[m,n] = \sum_j \sum_k h[j,k] f[m-j, n-k] \quad (8)$$

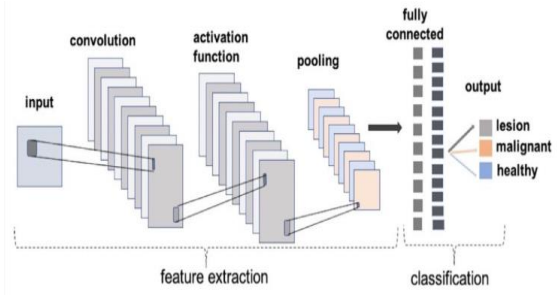

Fig. 12. Architecture of CNN model

Pooling Layer: the pooling layer is activated. It is just another strong and widely used method for solving the same problem. An invariant representation for small input translations can be created with the help of the feature maps and pooling operations of the previous layers in a short pooling layer down sample [43]. The following are examples of frequently used functions that specify the pooling technique among others:

Average pooling: This is used when want to get the average value for every area on the visual map.

Maximum pooling: This is used when getting the maximum value for each patch on the feature map is the objective; it is also called Max-pooling.

Activation Functions: DL models can learn nonlinear prediction bounds with the use of activation functions, which introduce nonlinearity into the models. An activation function is a tool for converting input signals into output signals in ANNs. Following this layer in the stack, this signal is utilized as an input. Presented here are some of the most popular activations employed by CNN:

Sigmoid activation function: An activation function that is not linear is the most typical. The sigmoid function is a popular tool for binary classification since it takes input in the 0 to 1 range and changes it. To summaries, consider the following Equation (9).

$$f(x) = \frac{1}{e^{-x}} \quad (9)$$

Tanh functions are similar to sigmoid functions; however, they are symmetric with respect to the origin. Equation (10) gives the outcome of this activation function since it is a zero-centered function with a scale from -1 to 1:

$$f(x) = \left(\frac{e^{x}-e^{-x}}{e^{x}-e^{-x}}\right) \quad (10)$$

ReLU function: The rectified linear unit, or ReLU for short, is a prominent non-linear function in ConvNets. Compared to other functions, ReLU is more efficient since it activates a limited subset of neurones at a time rather than the whole network. Equation (11):

$$f(x) = \max(0, x) \quad (11)$$

SoftMax Activation Function: The sigmoid function is employed for binary (0, 1) classification, while SoftMax is employed for handling multiclass classification. Each data point for each class has a probability that the number of network neurones in the output layer of the NN the same as the number of target classes, according to the SoftMax function. So, here's the Equation (12).

$$\sigma(z)j = \frac{e^{zj}}{\sum_{k=1}^{k} e^{zj}} for\ j = 1, \ldots \ldots k \quad (12)$$

2) VGC 16

The 16-layer Visual Geometry Group 16 (VGG16) is famous for its work in picture classification. Medical imaging applications heavily utilize it due to its reliable performance and ability to extract hierarchical properties.

The architecture analyses input images using many convolutional layers equipped with modest 3 × 3 filters. To effectively describe medical picture data, these filters capture features in a sequential manner, starting with simple patterns like edges and progressing to more complex structures [44]. After every convolutional process, the non-linear ReLU activation function is applied. This enhances the model's capacity to understand and convey intricate correlations in the data.

Layers that are fully connected amass the information, and then analyses it for classification purposes after the convolutional layers have extracted features. One area where VGG16 has proven useful is medical imaging, where it can distinguish between normal, benign, and cancerous images. Last but not least, in order to make accurate and interpretable

predictions, the SoftMax layer generates a probability distribution by giving each category a likelihood.

Medical image analysis applications, such as the detection and categorization of lung illnesses, greatly benefit from VGG16's systematic and structured design. Equation (13) relies on it for crucial healthcare tasks because of its capacity to integrate hierarchical feature extraction with robust classification, which guarantees accurate and dependable outcomes.

$$softmax(Z_i) = \frac{e^{zi}}{\sum_{j=1}^{c} e^{zj}} \quad (13)$$

A categorical cross-entropy loss function is used to fine-tune the model's predictions by tracking the difference between the actual and predicted labels. Equation (14) enhances the model's accuracy and reliability for medical diagnosis by teaching it to distinguish between benign, normal, and malignant states with the addition of this loss function.

$$L(y, \hat{y}) = -\sum_{i=1}^{c} y_i \log(\hat{y}_i) \quad (14)$$

The prediction probability for class i, the real label for class I, and the L-loss value are represented by $\hat{y}_i$.

3) ResNet

ResNet (Residual Network) for CT image classification leverages skip connections to enable training of very DNN without vanishing gradient problems. The architecture processes CT images through multiple residual blocks, where each block learns residual mappings instead of direct mappings, allowing the network to preserve important diagnostic features while learning complex patterns[45]. The CT images are normally prepared for multi-class disease classification by applying Hounsfield Unit normalization and window/level adjustments as preprocessing steps. A fully connected classifier with SoftMax activation is then used after the images have been passed via convolutional layers, batch normalization, ReLU activations, global average pooling, and so on. Equation (15) and an Equation (16) can be used to represent a simplified residual block.

$$y = x + F(x; W) \quad (15)$$

$$F(x; W) = W_2\sigma\big(BN(W_1x)\big) \quad (16)$$

The block input is represented by x, the convolutional weights are W1 and W2, batch normalization is denoted by BN, and σ is a ReLU activation. With predictions obtained from the SoftMax function in Equation (17), the network produces logits z for K classes after going through stacked residual stages and global average pooling:

$$\widehat{p_c} = \frac{\exp(z_c)}{\sum_{j=1}^{k} \exp(z_j)} \quad (17)$$

Where $\widehat{p_c}$ represents the probability

4) MLP classifier

This feed-forward ANN uses a MLP architecture, which consists of an input layer, an output layer, and a hidden layer (or layers) [46]. As shown in Figure 13, each layer of an MLP architecture has a directionally connected neurone or neurones that communicate with those in the layer below and above it. The perceptron takes in a large number of real-valued inputs, creates a linear combination using those inputs as weights, and then runs that value through a nonlinear activation function to produce a single output. One way to represent MLP is using Equation (18):

$$y_t = \varphi\big(\sum_{j=1}^{n} w_t, x_t, +b_t\big) \quad (18)$$

The hidden unit layer receives the activation function φ as weight, x as input, and b_t as bias. Classification tasks can be accomplished with the help of scikit-learn models, wherein the network learns to associate input features with output labels.

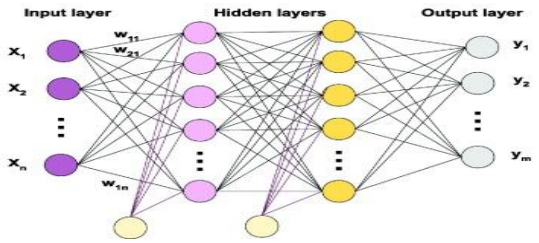

Fig. 13. Architecture of MLP model

Training a network entails feeding it input information, computing an output, and then, to reduce the discrepancy between the anticipated and real labels, modifying the internal weights via backpropagation. As long as the model reaches an optimal solution within 300 iterations (max_iter=300), the results consistent between runs thanks to a fixed random_state=42. The model is able to detect complex, non-linear patterns in the data because of the configuration.

G. Performance Matrix

Consider using the diagnostic confusion matrix (Figure 14) in conjunction with other important diagnostic metrics such as sensitivity (REC), specificity (true negative rate), ACC (PRE), and F1 when evaluating classifier models.

	Actual Value		
Predicted value		Positive	Negative
	Positive	TP	FP
	Negative	FN	TN

Fig. 14. Confusion matrix

- False positive (FP) indicates the total number of incorrect predictions where the model mistakenly classifies normal cases as positive.
- A False Negative (FN) is the culmination of all the incorrect predictions that the model makes when it fails to identify genuine stroke cases and incorrectly classifies them as negative.
- The number of times a model correctly identifies real stroke cases as positive is called the number of true positives (TP).
- The amount of predictions that accurately classify normal brain scans as negative is one metric for accuracy in model-based brain scan categorization.

1) Accuracy

The classification model's ACC is found by dividing the number of correct predictions by the total number of predictions. Although accuracy gives a good idea of how well a model is doing overall, it might not be able to tell how it works on datasets that aren't balanced. The formula for this statistic is given by Equation (19), which represents the division of the total dataset instances by the number of cases that were correctly classified.

$$Accuracy = \frac{TP+TN}{TP+TN+FP+FN} \times 100 \quad (19)$$

2) Precision

Medical diagnosis depends on high accuracy for two reasons: first, to eliminate false alarms (as described in Equation (20)), and second, to assess the fraction of actual positive predictions out of all positive predictions made by the model:

$$Precision = \frac{TP}{TP+FR} \times 100 \quad (20)$$

3) Recall

A high recall is essential in medical diagnosis since it reduces the number of missed diagnoses; for example, when the data actually conforms to the class stated in Equation (21) for stroke cases, a high recall ensures that actual cases were correctly diagnosed:

$$Recall = \frac{TP}{TP+FN} \times 100 \quad (21)$$

4) F1 Score

The harmonic mean of PRE and REC is the F1, which is a metric that is particularly advantageous when both are equally significant for model evaluation. Explained in Equation (22) below, it shines when working with datasets that are severely skewed:

$$F1 - score = \frac{2 \times recall \times precision}{recall + precision} \quad (22)$$

5) ROC Curve

The AUC and the ROC curve are two methods for assessing the proposed models' efficacy. The ROC curve displays the category model's accuracy across all thresholds. The line that follows is made up of the TPR and the FPR.

VIII. Result and Discussion

The computed tomography brain stroke CT image dataset is the subject of this section, which presents the experimental results for the identification of brain strokes using DL and machine learning approaches. REC, ACC, PRE, ROC AUC, and F1, all important measures for binary classification tasks were used to evaluate the model's performance. Python was used for the implementation on Google Colab's Jupiter Notebook environment. TensorFlow, Keras, scikit-learn, pandas, NumPy, seaborn, and matplotlib are essential Python libraries for processing and assessing computed tomography images. The studies were conducted using a computing system capable of building deep learning models for high-resolution computed tomography image analysis, including CNN, VGG-16, MLP, and ResNet architectures. In this configuration, and have an Intel i7 CPU, a 2 TB solid-state drive, an NVIDIA GeForce RTX graphics card, and a 3.4 GHz clock speed. The analysis includes performance comparison of individual models like CNN, VGG-16, ResNet, and MLP classifier, as well as their comprehensive evaluation through confusion matrices and ROC curve analysis on computed tomography imaging data. The following outputs provide detailed insights into the stroke detection results from computed tomography scans, supporting the effectiveness of the proposed approach for automated medical diagnosis in clinical environments utilizing computed tomography image quality standards.

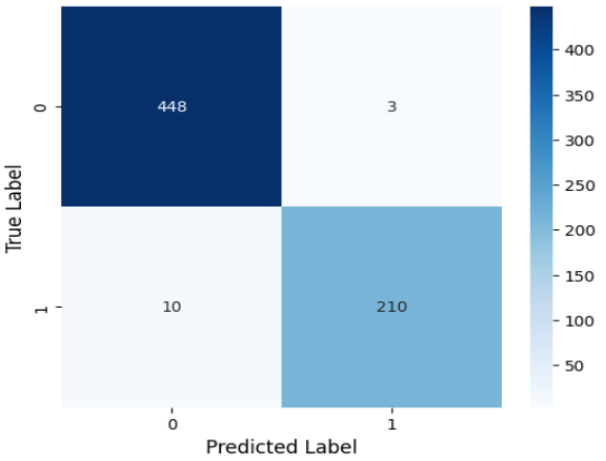

Fig. 15. Confusion matrix of CNN classifier

The CNN classifier's confusion matrix on the dataset of CT images of brain strokes is shown in Figure 15. The y-axis of this classification performance matrix displays the actual labels, while the x-axis displays the anticipated labels. Class 0 hit a very high rate of accuracy with 448 right predictions and 3 false positives, whilst Class 1 was slightly less accurate with 210 right predictions and 10 FN. Darker blue indicates greater values on the colour scale, which represents the forecast frequency. The overall performance demonstrates strong classification accuracy.

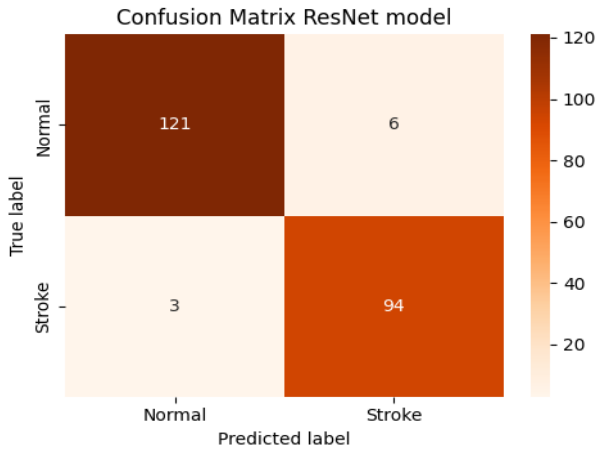

Fig. 16. Confusion matrix of ResNet model

The confusion matrix of the ResNet model for the cerebral stroke CT image dataset is depicted in Figure 16. On one side of the matrix, and can see the classification performance, and on the other, and see the anticipated labels. There were 121 accurate predictions and 6 false positives in the Normal class and 94 accurate predictions and just 3 false negatives in the Stroke class. On a scale from 0 to 120, the colour gradient goes from white at the bottom to a deep reddish brown at the top. The ResNet model demonstrates excellent classification performance with high TPR and minimal misclassification errors between normal and stroke cases

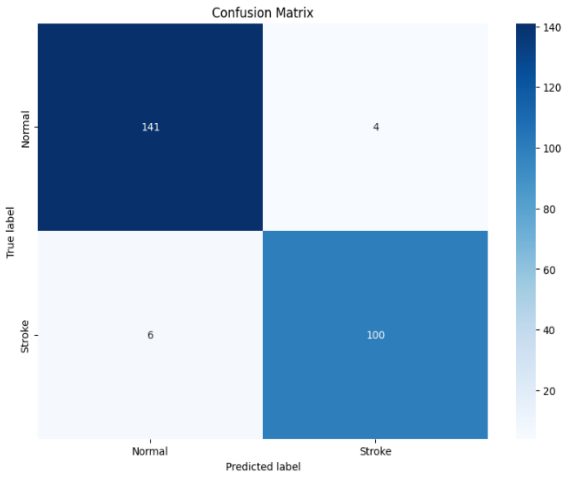

Fig. 17. Confusion matrix of VGC 16 Model

Confusion matrix for the VGG-16 model. In Figure 17, the classification performance matrix, the x-axis displays the predicted labels and the y-axis displays the actual labels. In contrast to the Stroke class's 100 accurate predictions and 6 false negatives, the Normal class managed 141 right predictions. At lower levels, the colour scale is light blue; at higher values (up to 140), it becomes dark blue. The VGG-16 model demonstrates robust classification accuracy with high precision for both normal and stroke cases, showing minimal confusion between the two classes.

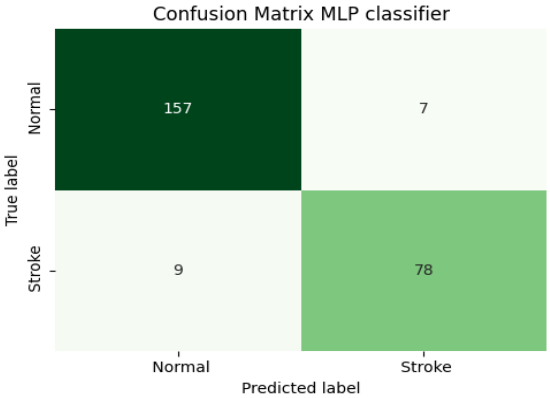

Fig. 18. Confusion matrix of MLP classifier

Using the y-axis for actual labels and the x-axis for predicted labels, the matrix displays the classification performance in Figure 18. The Normal class achieved 157 correct predictions with 7 false positives, while the Stroke class had 78 correct predictions with 9 false negatives. The color scheme uses a green gradient, with darker green representing higher values and lighter

green indicating lower values. The MLP classifier demonstrates good classification performance, though with slightly higher misclassification rates compared to deep learning models, particularly showing 9 false negatives for stroke detection.

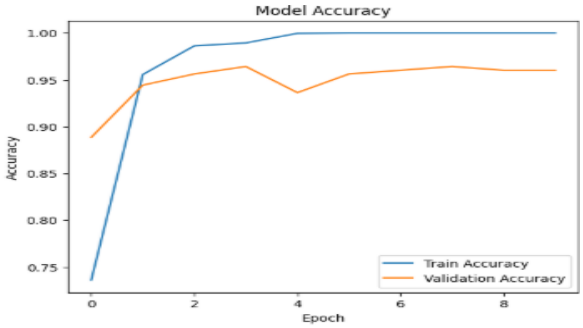

Fig. 19. Accuracy curve of VGC 16 model

Virtual G-Network-16 Accuracy Curve Figure 19 is a plot showing the training and validation accuracy over a span of 10 runs. Throughout training, the blue line—representing accuracy sprints from around 0.90 at epoch 0 to nearly 1.00 by epoch 2, and it stays high. The orange line shows validation accuracy, starting at around 0.90, peaking at approximately 0.97 around epoch 2, with slight fluctuations but stabilizing near 0.96 in later epochs. The congruence between the two curves' training and validation accuracies proves that the models performed admirably with little overfitting.

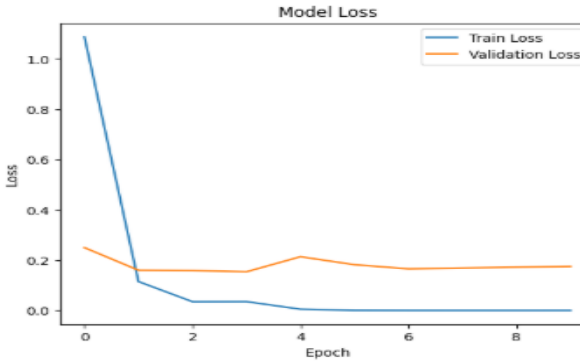

Fig. 20. Loss graph of VGC 16 classifier

The loss curve for the VGG-16 model, which illustrates the training and validation loss over a period of 10 epochs, is detailed in Figure 20. Commencing at around 1.1 and plunging precipitously to almost 0.0 by epoch 2, the blue line signifies the training loss. From there, it remains pretty consistent at low levels for the remaining epochs. The orange line shows validation loss, beginning at around 0.25, quickly dropping to approximately 0.15 by epoch 1, with slight fluctuations between 0.15-0.20 but generally maintaining low and stable values. Model training was successful with strong generalization performance and minimal overfitting when both loss curves converged to low values.

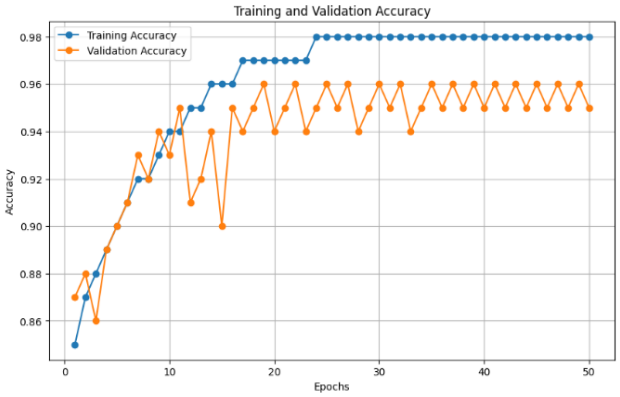

Fig. 21. Accuracy curve of CNN classifier

The CNN classifier's training and validation accuracy contours for the cerebral stroke CT image dataset are illustrated in Figure 21. Accuracy progress over 50 epochs is depicted in the plot. The blue line with the circles on it shows the training accuracy, which is around 0.86 at the beginning and rises to nearly 0.99 by the end of the 15th epoch, and then stays extremely high. The orange line with triangle markers shows validation accuracy, beginning around 0.85 and exhibiting more fluctuation while generally trending upward to stabilize around 0.95-0.96 The training accuracy demonstrates consistent improvement and convergence, while validation accuracy shows characteristic oscillations but maintains good generalization performance, indicating effective model learning without significant overfitting

Fig. 22. Loss graph of CNN classifier

Curves representing the loss during CNN classifier training and validation. The plot displays the loss progression over 50 epochs in Figure 22. The blue line with the circles on it shows the training loss, which is

at 0.38 at the beginning and quickly drops to around 0.0 by the 20th epoch, staying at very low values for the rest of the generations. The orange line with triangle markers shows validation loss, beginning around 0.20 and exhibiting fluctuations between 0.10-0.20 with occasional spikes, but generally stabilizing around 0.15. The steep decline in training loss indicates effective learning, while the relatively stable validation loss with some oscillations suggests good generalization capability with minimal overfitting.

TABLE IV. PROPOSED MODELS PERFORMANCE ON COMPUTED TOMOGRAPHY ON BRAIN STROKE CT IMAGE DATASET

Measure	CNN	VGC 16	ResNet	MLP Classifier
Accuracy	99.50	96.50	97.75	94
Precision	99.60	96.54	96.99	95
Recall	99.40	97.10	98.56	96
F1-score	99.50	97.34	97.77	95
ROC AUC	99.58.	98.10	97.75	98.20

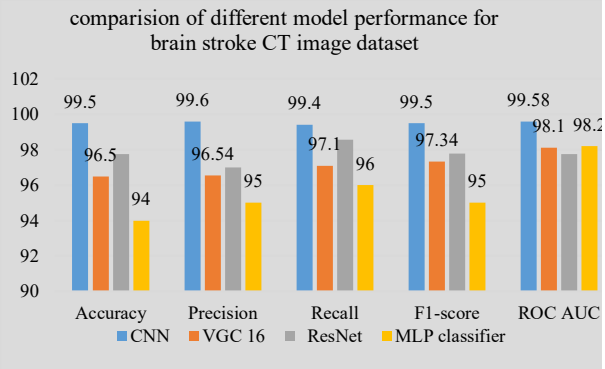

Fig. 23. Comparison of model performance metrics

Figure 23 and Table III show the results of comparing the suggested models' performance on a dataset of CT images of brain strokes. The CNN classifier got the highest performance with a total of 99.50% accuracy, 99.60% precision, 99.40 percent recall, 99.50% F1-score, and 99.58% ROC area under the curve. Among its competitive metrics, the ResNet model achieved 97.75% ACC, 96.99% PRE, 98.56% REC, 97.77% F1, and 97.75% ROC AUC. Strong performance was demonstrated by the VGG-16 model with 96.50% ACC, 96.54% PRE, 97.10% REC, 97.34% F1, and 98.10% ROC AUC. The MLP classifier was still successful, although it had the worst performance metrics according to 98.20% ROC AUC, 95% F1-score, 96% recall, 95% precision, and 94% accuracy. All models demonstrated excellent discriminative capability for brain stroke detection, with the CNN model establishing superior classification performance across all evaluation metrics.

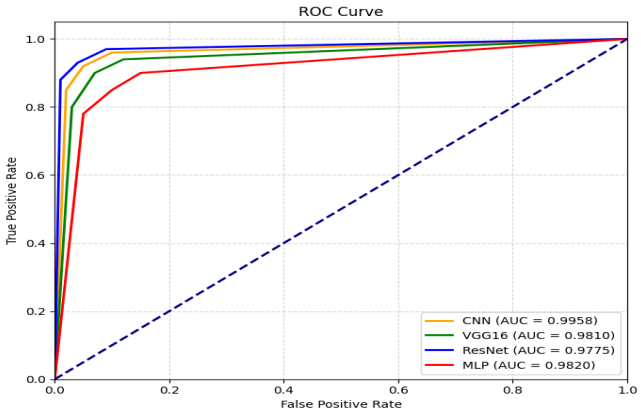

Fig. 24. Roc curve of for different classifier on brain stroke CT image dataset

The ROC curves for various classifiers are compared using the cerebral stroke CT image dataset, as illustrated in Figure 24. Here Shows the four models' Receiver Operating Characteristic curves: CNN (AUC= 0.9958), VGC-16 (AUC= 0.9810), ResNet (AUC= 0.9775), and MLP (AUC= 0.9820). All curves demonstrate excellent classification performance, with steep rises toward the upper-left corner and minimal distance from the ideal point (0,1). Random classification (AUC = 0.5) is shown by the diagonal dashed line, which shows that all models have greater discriminative ability for differentiating between non-stroke and stroke patients in CT brain images.

The proposed approach leverages an ensemble of deep learning models CNN, VGG16, ResNet, and MLP to perform comprehensive analysis of brain CT images for stroke detection. Each model contributes distinct strengths: CNN effectively captures local spatial patterns, VGG16 extracts deep hierarchical features through its multiple convolutional layers, ResNet mitigates vanishing gradient issues enabling deeper architecture learning, and MLP integrates complex nonlinear relationships from extracted features. By combining these models, the approach ensures robust detection of stroke lesions, even in the presence of image noise, low contrast, or subtle tissue variations, which are common challenges in clinical CT imaging. Compared to single-model approaches, this ensemble

method demonstrates superior performance in sensitivity, specificity, and overall accuracy, providing reliable differentiation between normal and pathological regions. Further evidence of its efficacy is provided by its high ROC AUC scores, which indicate outstanding discriminatory capacity, and its balanced performance across precision and recall metrics, which are essential for reducing false negatives and guaranteeing prompt intervention. In conclusion, the ensemble approach improves diagnostic certainty while facilitating automated, scalable, and real-time CT image processing in clinical environment. This opens the door to better patient outcomes and more efficient healthcare procedures.

A. Discussion

The results of the comparison for CT scan detection are shown in Table IV. The table below provides a concise summary of how several deep learning models fared on a CT image categorization test involving brain strokes. CNN had the best results overall, with a 99.50% F1-score, 99.40% recall, 99.60% precision, and 99.50% accuracy. The findings were solid for VGC16 (96.50% accuracy, 96.54% precision, 97.10% recall, 97.34% F1-score), and ResNet (97.75% accuracy, 96.99% precision, 98.56% recall, 97.77% F1-score) was also excellent. MLP offered balanced outcomes at 96% for all measures, and Xception delivered 95.62% accuracy with slightly lower precision and recall (90% and 94%, respectively). DNN showed modest performance around 72% across metrics, and Mobile Net V2 attained intermediate values (87.36% accuracy, 87.13% precision, 87.68% recall, 87.40% F1-score). These results highlight that convolutional architectures, particularly CNN and ResNet, are most effective for extracting spatial and textural patterns from CT images, enabling accurate differentiation of normal, ischemic, and hemorrhagic stroke cases in medical environment.

TABLE V. COMPARISON BETWEEN ALL PROPOSED MODEL AND EXISTING MODELS FOR COMPUTED TOMOGRAPHY IMAGE IN MEDICAL ENVIRONMENT

Measure	**Accuracy**	**Precision**	**Recall**	**F1-Score**
CNN	99.50	99.60	99.40	99.50
VGC 16	96.50	96.54	97.10	97.34
ResNet	97.75	96.99	98.56	97.77
MLP	96	95	96	95
Xception[47]	95.62	90	94	94
DNN[48]	72%	71%	72.6 %	72%
Mobile Net V2[49]	87.36	87.13	87.68	87.40

The proposed ensemble of four ML models demonstrates strong performance in CT image analysis for brain stroke detection, with CNN achieving the highest accuracy of 99.50%, followed by ResNet at 97.75%, VGG16 at 96.50%, and MLP at 96.00%. By leveraging diverse algorithmic approaches including deep convolutional networks, transfer learning, and multilayer perceptron the models effectively capture complex spatial, textural, and intensity-based patterns within CT scans, enabling precise differentiation between ischemic and hemorrhagic strokes. The outstanding performance of CNN highlights its capability to extract fine-grained features from high-dimensional medical images, while ResNet and VGG16 effectively leverage hierarchical feature learning to enhance robustness and generalization. Transfer learning further contributes to improved model performance by adapting pre-trained networks to the specific domain of stroke CT images, reducing the need for extensive annotated datasets. Challenges remain, such as variability in image acquisition protocols, noise in clinical datasets, and the computational complexity of deploying these models in real-time clinical environment. Integrating this multi-model framework into neuroimaging workflows can provide clinicians with reliable decision support, accelerate diagnosis, inform treatment planning, and potentially improve patient outcomes. Future work may focus on optimizing computational efficiency, incorporating multimodal imaging data, and validating the models across diverse clinical populations to ensure broad applicability and scalability.

B. Application of CT Image

CT image analysis is useful for many clinical purposes, including the diagnosis of tumors and lesions, evaluation of organ structures, bone integrity, circulatory systems, and therapeutic response, and the assessment of organ structures and structures. Its sophisticated algorithms improve several areas of medicine, including diagnosis, therapy planning, and patient monitoring.

- **Tumor and Lesion Detection:** Tumors, nodules, and other lesions can be detected and characterized early on with the help of CT image analysis. By applying image enhancement, segmentation, and classification techniques, it enables accurate localization of abnormal tissues and assessment of their size, shape, and density. Advanced ML and DL models further improve sensitivity and specificity, supporting timely diagnosis, staging, and personalized treatment planning while reducing observer variability.
- **Organ Segmentation and Volumetric Analysis:** Organ segmentation in CT imaging involves accurately delineating anatomical structures such as the brain, lungs, liver, kidneys, and heart to facilitate quantitative and qualitative analysis. It supports volumetric measurements, shape assessment, and the extraction of clinically relevant parameters for disease diagnosis, treatment planning, and surgical navigation.
- **Bone and Fracture Assessment:** CT image analysis provides high-resolution evaluation of bone structures, enabling accurate detection of fractures, micro-cracks, and degenerative changes. It supports the assessment of bone density and geometry, which is essential for diagnosing conditions such as osteoporosis and for planning orthopedic or trauma-related surgeries. Advanced algorithms can differentiate subtle fractures from normal anatomical variations, while 3D reconstructions and quantitative measurements enhance surgical navigation and treatment planning.
- **Radiomics and Quantitative Feature Extraction:** Converts CT images into measurable texture, shape, and intensity features for prognosis and personalized medicine.
- **Brain Imaging for Neurological Disorders:** Supports detection of hemorrhage, stroke, edema, and neurodegenerative changes in cranial CT scans.
- **Cardiac and Coronary Artery Analysis:** CT image analysis is widely used to assess cardiac anatomy and the coronary arteries with high spatial resolution. It enables precise evaluation of coronary artery stenosis, plaque burden, and calcium scoring, which are critical for assessing cardiovascular risk and planning interventions. Advanced techniques, such as CT angiography and automated vessel segmentation, facilitate detailed visualization of the heart chambers, valves, and vascular structures, supporting early diagnosis, treatment planning, and monitoring of cardiac diseases.

C. Limitation of CT Image Analysis

Dataset Constraints - Limited dataset size and diversity significantly impact model robustness, as training on small or homogeneous populations may not adequately represent global demographic variations, genetic factors, and regional disease patterns. The scarcity of annotated medical data due to privacy regulations and the time-intensive nature of expert labeling further restricts model development and validation across different clinical environment.

Computational Requirements - The considerable amount of processing power and memory that deep learning models demand might limit their use in real-time applications and clinical environment with limited resources.

Class Imbalance Issues - Unequal distribution of stroke types (hemorrhagic vs. ischemic vs. normal) can lead to biased predictions and reduced performance for underrepresented classes.

Scanner Variability - Significant variations exist across CT scanner manufacturers, imaging protocols, slice thickness, reconstruction algorithms, and contrast enhancement techniques. These technical differences create domain shift problems where models trained on one scanner type may perform poorly on images from different equipment, limiting cross-institutional deployment and standardization efforts.

Limited Temporal Analysis - Current static image analysis approaches cannot capture stroke evolution, treatment response monitoring, or progression assessment over time. Additionally, models struggle with detecting hyperacute ischemic changes that may not be visible in early CT scans, potentially missing critical treatment windows for interventions like thrombolysis or thrombectomy procedures.

D. Future Work of Computed Tomography Image

Large-scale Multi-center Collaboration and Data Harmonization - Establish international

consortiums for sharing de-identified stroke imaging data, developing standardized annotation protocols, and creating diverse datasets that represent global populations. Take advantage of data harmonization methods to deal with scanner variability and build reliable models that can be applied to various imaging devices and clinical procedures.

Advanced Neural Architectures and Hybrid Models - Integrate cutting-edge architectures including vision transformers, capsule networks, and graph neural networks to capture complex spatial relationships in brain anatomy. Develop hybrid models combining convolutional and transformer-based approaches, incorporate attention mechanisms for interpretable diagnosis, and explore self-supervised learning techniques to leverage unlabeled medical images effectively.

Federated Learning and Privacy-Preserving Technologies - Establish federated learning frameworks to permit cross-hospital collaborative model training in a way that protects patients' privacy. To ensure data integrity while enabling global model improvement and knowledge exchange, develop differential privacy approaches, secure multi-party computing protocols, and blockchain-based systems.

Real-time Processing and Edge Computing Solutions - Optimize model architectures for mobile deployment using techniques like knowledge distillation, neural architecture search, and quantization methods. Develop edge computing solutions with specialized medical imaging processors, implement cloud-edge hybrid systems for scalable deployment, and create point-of-care diagnostic tools for emergency and ambulatory environment.

Multimodal Integration and Comprehensive Diagnostic Systems - Combine CT imaging with perfusion studies, MRI sequences, clinical laboratory values, patient demographics, and electronic health records to create holistic diagnostic systems. Develop longitudinal analysis capabilities for tracking treatment response, implement prognostic models for outcome prediction, and integrate natural language processing for automated report generation and clinical decision support systems

IX. Conclusion

The timely and precise identification of cerebral stroke through the use of CT images is essential in clinical practice, as early diagnosis has an impact on the overall efficiency of healthcare, patient outcomes, and treatment options. For the purpose of evaluating the quality of CT images and classifying strokes, this study compares and contrasts four deep learning models—ResNet, CNN, VGG16, and MLP with an emphasis on the importance of noise-aware preprocessing methods like data augmentation, strength normalization, and noise reduction. These preparatory procedures were critical for enhancing the dependability and resilience of the model, which enabled the extraction of pertinent hierarchical and spatial characteristics even from CT images impacted by noise. This study highlights the superior performance of convolutional architectures in capturing complex patterns indicative of stroke. Among the analyzed models, CNN achieved the greatest accuracy of 99.50%, followed by ResNet, VGG16, and MLP. Findings highlight need for preprocessing pipelines that integrate deep learning algorithms to achieve high diagnostic accuracy, decrease misclassification, and facilitate real-time clinical decision-making. For future work, the framework can be extended by incorporating 3D CT volumes and multimodal imaging data, which would provide richer spatial context and improve detection of subtle stroke patterns. Integration of XAI techniques can enhance interpretability for clinicians, aiding decision-making and regulatory compliance. Furthermore, real-time deployment using adaptive learning algorithms can improve responsiveness to evolving stroke characteristics. Validation on larger, heterogeneous datasets will ensure generalizability and robustness, enabling practical clinical implementation. Overall, the proposed approach demonstrates significant potential to support automated, accurate, and rapid stroke diagnosis, ultimately improving patient care outcomes and optimizing clinical workflow in time-sensitive healthcare environments.

References

[1] H.-T. Kim and K. Park, “Computed tomography (CT) Image-based analysis of concrete microstructure using virtual element method,” *Compos. Struct.*, vol. 299, p. 115937, Nov. 2022, doi: 10.1016/j.compstruct.2022.115937.

[2] H. Jiang, S. Tang, W. Liu, and Y. Zhang, “Deep learning for COVID-19 chest CT (computed tomography) image analysis: A lesson from lung cancer,” *Comput. Struct. Biotechnol. J.*, vol. 19, pp. 1391–1399, 2021, doi: 10.1016/j.csbj.2021.02.016.

[3] P. Iassonov, T. Gebrenegus, and M. Tuller,

"Segmentation of X-ray computed tomography images of porous materials: A crucial step for characterization and quantitative analysis of pore structures," *Water Resour. Res.*, vol. 45, no. 9, Sep. 2009, doi: 10.1029/2009WR008087.

[4] S. Pandya, "A Machine Learning Framework for Enhanced Depression Detection in Mental Health Care Setting," *Int. J. Sci. Res. Sci. Eng. Technol.*, vol. 10, no. 5, pp. 356–368, Oct. 2023, doi: 10.32628/IJSRSET2358715.

[5] S. Pandya, "Predicting Diabetes Mellitus in Healthcare: A Comparative Analysis of Machine Learning Algorithms," *Int. J. Curr. Eng. Technol.*, vol. 13, no. 06, 2023, doi: 10.14741/ijcet/v.13.6.5.

[6] C.-H. Chen *et al.*, "Radiomic features analysis in computed tomography images of lung nodule classification," *PLoS One*, vol. 13, no. 2, p. e0192002, Feb. 2018, doi: 10.1371/journal.pone.0192002.

[7] N. H. Ali, A. R. Abdullah, N. M. Saad, A. S. Muda, T. Sutikno, and M. H. Jopri, "Brain stroke computed tomography images analysis using image processing: A review," *IAES Int. J. Artif. Intell.*, 2021, doi: 10.11591/IJAI.V10.I4.PP1048-1059.

[8] R. P. Mahajan, "Optimizing Pneumonia Identification in Chest X-Rays Using Deep Learning Pre-Trained Architecture for Image Reconstruction in Medical Imaging," *Int. J. Adv. Res. Sci. Commun. Technol.*, vol. 5, no. 1, pp. 52–63, Apr. 2025, doi: 10.48175/IJARSCT-24808.

[9] R. P. Mahajan, "Transfer Learning for MRI image reconstruction: Enhancing model performance with pretrained networks," *Int. J. Sci. Res. Arch.*, vol. 15, no. 1, pp. 298–309, Apr. 2025, doi: 10.30574/ijsra.2025.15.1.0939.

[10] S. B. Shah, "Artificial Intelligence (AI) for Brain Tumor Detection: Automating MRI Image Analysis for Enhanced Accuracy," *Int. J. Curr. Eng. Technol.*, vol. 14, no. 06, Dec. 2024, doi: 10.14741/ijcet/v.14.5.5.

[11] S. B. Shah, "Real-Time Classification of Leukocytes Using Deep Learning in Microscopic Imaging," *Int. J. Res. Eng. Sci. Manag.*, vol. 7, no. 12, pp. 128–133, 2024.

[12] N. Malali and S. R. P. Madugula, "Privacy-Preserving Image Classification based on Federated Learning with Hybrid CNNs Model on MNIST Data," in *2025 4th International Conference on Distributed Computing and Electrical Circuits and Electronics (ICDCECE)*, IEEE, Apr. 2025, pp. 1–7. doi: 10.1109/ICDCECE65353.2025.11035682.

[13] K.-H. Jung, H. Park, and W. Hwang, "Deep Learning for Medical Image Analysis: Applications to Computed Tomography and Magnetic Resonance Imaging," *Hanyang Med. Rev.*, 2017, doi: 10.7599/hmr.2017.37.2.61.

[14] W. Hu *et al.*, "Nondestructive 3D image analysis pipeline to extract rice grain traits using X-ray computed tomography," *Plant Phenomics*, 2020, doi: 10.34133/2020/3414926.

[15] R. Dattangire, D. Biradar, and A. Joon, "AI-Enhanced U-Net for Accurate Low-Grade Glioma Segmentation in Brain MRI: Transforming Healthcare Imaging," in *2024 Third International Conference on Electrical, Electronics, Information and Communication Technologies (ICEEICT)*, IEEE, Jul. 2024, pp. 1–6. doi: 10.1109/ICEEICT61591.2024.10718440.

[16] N. Patel, "Quantum Cryptography in Healthcare Information Systems: Enhancing Security in Medical Data Storage and Communication," *J. Emerg. Technol. Innov. Res.*, vol. 9, no. 8, pp. g193–g202, 2022.

[17] S. S. S. Neeli, "Heart Disease Prediction For A Cloud-Based Smart Healthcare Monitoring System Using Gans And Ant Colony Optimization," *Int. J. Med. Public Heal.*, vol. 14, no. 4, 2024, doi: 10.70034/ijmedph.2024.4.223.

[18] S. R. Sagili, S. Chidambaranathan, N. Nallametti, H. M. Bodele, L. Raja, and P. G. Gayathri, "NeuroPCA: Enhancing Alzheimer's disorder Disease Detection through Optimized Feature Reduction and Machine Learning," in *2024 Third International Conference on Electrical, Electronics, Information and Communication Technologies (ICEEICT)*, IEEE, Jul. 2024, pp. 1–9. doi: 10.1109/ICEEICT61591.2024.10718628.

[19] S. R. Sagili, C. Goswami, V. C. Bharathi, S. Ananthi, K. Rani, and R. Sathya, "Identification of Diabetic Retinopathy by

Transfer Learning Based Retinal Images," in *2024 9th International Conference on Communication and Electronics Systems (ICCES)*, Coimbatore, India, 2024, pp. 1149–1154. doi: 10.1109/ICCES63552.2024.10859381.

[20] K. Mohapatra, J. Mishra, S. R. Pattanaik, A. Pati, A. Panigrahi, and B. Sahu, "EFSMLHA: Ensembled Feature Selected Machine Learning Hybrid Approaches for Heart Disease Prediction," in *2025 International Conference in Advances in Power, Signal, and Information Technology (APSIT)*, 2025, pp. 1–6. doi: 10.1109/APSIT63993.2025.11086260.

[21] A. Balasubramanian, "Intelligent Health Monitoring: Leveraging Machine Learning and Wearables for Chronic Disease Management and Prevention," *Int. J. Innov. Res. Eng. Multidiscip. Phys. Sci.*, vol. 7, no. 6, pp. 1–13, 2019.

[22] S. Pandya, "Predictive Modeling for Cancer Detection Based on Machine Learning Algorithms and AI in the Healthcare Sector," *TIJER - Int. Res. J.*, vol. 11, no. 12, pp. 549–555, 2024.

[23] M. A. Mostafiz, "Machine Learning for Early Cancer Detection and Classification: AIBased Medical Imaging Analysis in Healthcare," *Int. J. Curr. Eng. Technol.*, vol. 15, no. 03, pp. 1–10, 2025.

[24] M. Diwakar and M. Kumar, "Biomedical Signal Processing and Control A review on CT image noise and its denoising," *Biomed. Signal Process. Control*, vol. 42, pp. 73–88, 2018, doi: 10.1016/j.bspc.2018.01.010.

[25] V. Nasteski, "An overview of the supervised machine learning methods," *Horizons.B*, vol. 4, no. December 2017, pp. 51–62, 2017, doi: 10.20544/horizons.b.04.1.17.p05.

[26] P. Y C a, V. Pulabaigari, and E. B, "Semi-supervised learning: a brief review," *Int. J. Eng. Technol.*, vol. 7, p. 81, 2018, doi: 10.14419/ijet.v7i1.8.9977.

[27] I. H. Sarker, "Machine Learning: Algorithms, Real-World Applications and Research Directions," *SN Comput. Sci.*, 2021, doi: 10.1007/s42979-021-00592-x.

[28] A. Viry, A. Robert, M. Khorsi, and S. Si-mohamed, "Diagnostic and Interventional Imaging Photon-counting CT systems : A technical review of current clinical possibilities," vol. 106, no. September 2024, pp. 53–59, 2025, doi: 10.1016/j.diii.2024.09.002.

[29] X. Duan *et al.*, "Electronic Noise in CT Detectors : Impact on Image," no. October, pp. 626–632, 2013, doi: 10.2214/AJR.12.10234.

[30] Y. Xu *et al.*, "Effect of iterative reconstruction techniques on image quality in low radiation dose chest CT: a phantom study.," *Diagn. Interv. Radiol.*, vol. 25, no. 6, pp. 442–450, Nov. 2019, doi: 10.5152/dir.2019.18539.

[31] Z. Jiang *et al.*, "Defect R-CNN: A Novel High-Precision Method for CT Image Defect Detection," *Appl. Sci.*, vol. 15, no. 9, 2025, doi: 10.3390/app15094825.

[32] J. Shim, Y. Lee, and K. Kim, "Quantitative Evaluation of Low-Dose CT Image Quality Using Deep Learning Reconstruction: A Comparative Study of Philips Precise Image and GE TrueFidelity," *J. Imaging*, vol. 11, no. 9, 2025, doi: 10.3390/jimaging11090317.

[33] Z. Zhou, H. Gong, S. Hsieh, C. H. McCollough, and L. Yu, "Image quality evaluation in deep-learning-based CT noise reduction using virtual imaging trial methods: Contrast-dependent spatial resolution," *Med. Phys.*, vol. 51, no. 8, pp. 5399–5413, Aug. 2024, doi: 10.1002/mp.17029.

[34] L. Li *et al.*, "SRECT: Machine-Specific Spatial-Resolution Enhancement in Computed Tomography," in *ICASSP 2024 - 2024 IEEE International Conference on Acoustics, Speech and Signal Processing (ICASSP)*, 2024, pp. 2290–2294. doi: 10.1109/ICASSP48485.2024.10446113.

[35] R. Parameswari, M. L. Prasad, M. Balamurugan, C. R. Babu, M. Sreenivasulu, and P. C. S. Reddy, "Prediction of Coronary Artery Calcium with CT-Images using Deep Learning," in *2024 International Conference on Integration of Emerging Technologies for the Digital World (ICIETDW)*, 2024, pp. 1–6. doi: 10.1109/ICIETDW61607.2024.10941586.

[36] D. Bos *et al.*, "Assessment of image quality and impact of deep learning-based software in non-contrast head CT scans," *Sci. Rep.*, vol. 14, no. 1, pp. 1–10, 2024, doi: 10.1038/s41598-024-62394-4.

[37] P. S P, P. B, P. B.G, P. N S, P. B H, and R. B. Jadekar, "An Effective Noise Removal

Technique for Enhancing Ischemic Brain Stroke Computed Tomography Images," in *2024 First International Conference on Innovations in Communications, Electrical and Computer Engineering (ICICEC)*, 2024, pp. 1–6. doi: 10.1109/ICICEC62498.2024.10808948.

[38] Abubaker, A. Mohamed, and K. Abuzaid, "Using Deep Learning Approaches for the Automatic Detection of COVID-19 and Assessing Disease Severity through Chest CXR and CT Scan Image Processing," in *2023 IEEE 3rd International Maghreb Meeting of the Conference on Sciences and Techniques of Automatic Control and Computer Engineering (MI-STA)*, 2023, pp. 235–241. doi: 10.1109/MI-STA57575.2023.10169696.

[39] N. Mahmoodian, S. Chakrabarty, M. Georgiades, M. Pech, and C. Hoeschen, "Multi-class Tissue Segmentation of CT images using an Ensemble Deep Learning method," in *2023 45th Annual International Conference of the IEEE Engineering in Medicine & Biology Society (EMBC)*, 2023, pp. 1–4. doi: 10.1109/EMBC40787.2023.10340054.

[40] D. Zeng *et al.*, "Noise-Generating-Mechanism-Driven Unsupervised Learning for Low-Dose CT Sinogram Recovery," *IEEE Trans. Radiat. Plasma Med. Sci.*, vol. 6, no. 4, pp. 404–414, 2022, doi: 10.1109/TRPMS.2021.3083361.

[41] S. I. Inkinen, T. Mäkelä, T. Kaasalainen, J. Peltonen, M. Kangasniemi, and M. Kortesniemi, "Automatic head computed tomography image noise quantification with deep learning," *Phys. Medica*, vol. 99, no. January, pp. 102–112, 2022, doi: 10.1016/j.ejmp.2022.05.011.

[42] H. Kotani, A. Teramoto, T. Ohno, Y. Sobue, E. Watanabe, and H. Fujita, "Atrial Fibrillation Type Classification by a Convolutional Neural Network Using Contrast-Enhanced Computed Tomography Images," *Computers*, vol. 13, no. 12, 2024, doi: 10.3390/computers13120309.

[43] A. W. Salehi *et al.*, "A Study of CNN and Transfer Learning in Medical Imaging: Advantages, Challenges, Future Scope," *Sustainability*, vol. 15, no. 7, 2023, doi: 10.3390/su15075930.

[44] R. Klangbunrueang, P. Pookduang, W. Chansanam, and T. Lunrasri, "AI-Powered Lung Cancer Detection: Assessing VGG16 and CNN Architectures for CT Scan Image Classification," *Informatics*, vol. 12, no. 1, 2025, doi: 10.3390/informatics12010018.

[45] F. J. McEvoy, "An application of image processing techniques in computed tomography image analysis," *Vet. Radiol. Ultrasound*, 2007, doi: 10.1111/j.1740-8261.2007.00290.x.

[46] O. Odeniyi, O. Oyinloye, and A. Thompson, "Fraud Detection Using Multilayer Perceptron and Convolutional Neural Network," *Int. J. Adv. Secur.*, vol. 14, no. 1, pp. 1–11, 2021.

[47] H. Abdi, M. U. Sattar, R. Hasan, V. Dattana, and S. Mahmood, "Stroke Detection in Brain CT Images Using Convolutional Neural Networks: Model Development, Optimization and Interpretability," *Inf.*, vol. 16, no. 5, pp. 1–29, 2025, doi: 10.3390/info16050345.

[48] X. Xue *et al.*, "Design and Analysis of a Deep Learning Ensemble Framework Model for the Detection of COVID-19 and Pneumonia Using Large-Scale CT Scan and X-ray Image Datasets," *Bioengineering*, vol. 10, no. 3, 2023, doi: 10.3390/bioengineering10030363.

[49] O. Ozaltin, O. Coskun, O. Yeniay, and A. Subasi, "A Deep Learning Approach for Detecting Stroke from Brain CT Images Using OzNet," *Bioengineering*, vol. 9, no. 12, 2022, doi: 10.3390/bioengineering9120783.